Accepted for publication in The Astronomical Journal

Environment, Ram Pressure, and Shell Formation in HoII

M. Bureau[1,2]
Sterrewacht Leiden, Postbus 9513, 2300 RA Leiden, The Netherlands;
bureau@strw.leidenuniv.nl

and

C. Carignan
Département de Physique and Observatoire du Mont Mégantic, Université de Montréal,
C. P. 6128, Succ. "centre-ville", Montréal, Québec, Canada H3C 3J7;
carignan@astro.umontreal.ca

ABSTRACT

Neutral hydrogen VLA D-array observations of the dwarf irregular galaxy HoII, a prototype galaxy for studies of shell formation, are presented. These were extracted from the multi-configuration dataset of Puche et al. (1992). H I is detected to radii over $16'$ or $4R_{25}$, almost a factor of two better than previous studies. The total H I mass $M_{\rm HI} = 6.44 \times 10^8\ M_\odot$. The integrated H I map has a comet-like appearance, with a large but faint component extending to the northwest and the H I appearing compressed on the opposite side. This suggests that HoII is affected by ram pressure from an intragroup medium (IGM). The velocity field shows a clear rotating disk pattern and a rotation curve corrected for asymmetric drift was derived. However, the gas at large radii may not be in equilibrium. Puche et al. (1992) multi-configuration data were also reanalyzed and it is shown that they overestimated their fluxes by over 20%.

The rotation curve derived for HoII is well defined for $r \lesssim 10$ kpc. For $10 \lesssim r \lesssim 18$ kpc, however, velocities are only defined on the approaching side, such that this part of the rotation curve should be used with caution. An analysis of the mass distribution, using the whole extent of this rotation curve,

---

[1]Hubble Fellow

[2]Now at: Columbia Astrophysics Laboratory, 550 West 120th Street, 1027 Pupin Hall, Mail Code 5247, New York, NY 10027, U.S.A.

yields a total mass of $6.3 \times 10^9\ M_\odot$, of which $\approx 80\%$ is dark. Similarly to what is seen in many dwarfs, there is more luminous mass in H I than in stars. One peculiarity, however, is that luminous matter dominates within the optical body of the galaxy and dark matter only in the outer parts, analogous to what is seen in massive spirals rather than dwarfs.

HoII lies northeast of the M81 group's core, along with Kar 52 (M81 Dwarf A) and UGC 4483. No signs of interaction are observed, however, and it is argued that HoII is part of the NGC 2403 subgroup, infalling towards M81. A case is made for ram pressure stripping and an IGM in the M81 group. Stripping of the outer parts of the disk would require an IGM density $n_{\rm IGM} \gtrsim 4.0 \times 10^{-6}$ atoms cm^{-3} at the location of HoII. This corresponds to $\sim$1% of the virial mass of the group uniformly distributed over a volume just enclosing HoII and it is consistent with the known X-ray properties of small groups. The H I tail is consistent with additional turbulent viscous stripping and evaporation, at least for low IGM temperatures.

It is argued that existing observations of HoII do not support self-propagating star formation scenarios, whereby the H I holes and shells are created by supernova explosions and stellar winds. Many H I holes are located in low surface density regions of the disk, where no star formation is expected or observed. Alternative mechanisms are discussed and it is suggested that ram pressure can help. Ram pressure has the capacity to enlarge preexisting holes and lower their creation energies, helping to bridge the gap between the observed star formation rate and that required to create the holes.

Subject headings: galaxies: individual (HoII) — galaxies: irregular — galaxies: structure — galaxies: kinematics and dynamics — galaxies: ISM — galaxies: intergalactic medium

1. Introduction

Spiral galaxies have a complex interstellar medium (ISM) pierced by numerous cavities. These were first identified in the Galaxy (Heiles 1979, 1984) and M31 (Brinks 1981; Brinks & Bajaja 1986), but similar structures were quickly discovered in other nearby galaxies (e.g. Deul & den Hartog 1990 for M33; Kamphuis 1993 for M101 and NGC 6946). The majority of these cavities are generally thought to arise from the combined effects of supernova explosions (SNe) and stellar winds (see Tenorio-Tagle & Bodenheimer 1988 and van der

Hulst 1996 for reviews), consistent with a three-phase picture of the ISM (Cox & Smith 1974; McKee & Ostriker 1977). In late-type spirals and dwarfs, cavities are long-lived due to a combination of low shear, a shallow gravitational potential, the absence of spiral density waves, and large scaleheights.

One of the best studied dwarf irregulars is without doubt HoII, in the nearby M81 group of galaxies. Its basic properties are listed in Table 1. Puche et al. (1992; hereafter PWBR92) cataloged and characterized over 50 H I holes and shells in HoII using multi-configuration observations from NRAO's Very Large Array[3] (VLA), arguing for sequential star formation events in the disk. This picture has since been criticized (e.g. Rhode et al. 1999), but it was already clear then that some holes required extremely high creation energies (up to 2×10^{53} ergs). PWBR92 pointed out that HoII probably contains some dark matter, but they commented only briefly on its large-scale mass distribution, although it may be crucial to understand the evolution of the shells and constrain the amount of gas expelled from the galaxy (e.g. Silich et al. 1996; Efstathiou 2000). PWBR92 detected a small H I cloud to the southwest, pointing to a significant amount of H I at large radii. This is essential to constrain the dark matter distribution, but also hints at a disturbed large-scale ISM or intergalactic medium (IGM). This is vindicated in our study, which shows that HoII has an extended comet-like H I morphology, possibly caused by ram pressure.

In this paper, we will focus on HoII's large-scale H I distribution, looking at how it can help us understand its current properties and unravel its evolutionary history. In § 2, we reanalyze and discuss PWBR92's data, using exclusively the low-resolution D-array observations. In § 3, we derive HoII's rotation curve and discuss its mass distribution. The likelihood of ram pressure and the properties of a putative IGM are discussed in § 4. In § 5, the creation of shells and supershells is discussed in light of all available observations. We summarize our results and briefly conclude in § 6.

2. Data Reduction and Analysis

The starting point for our analysis was the multi-configuration VLA data of PWBR92 (B, C, and D arrays; 1990 August 10, 1990 December 2, and 1991 March 6, respectively), which were kindly made available to us by Puche. We only briefly review here the calibration of the data and refer the reader to PWBR92 for a more extensive discussion. The flux calibration and complex bandpass corrections were provided by observations of 3C 286 in

[3]The National Radio Astronomy Observatory is a facility of the National Science Foundation operated under a cooperative agreement by Associated Universities, Inc.

each configuration and the amplitudes and phases were calibrated using 0859+681 and 0836+710, close to the source. The data were also edited to remove bad data points and the three *uv* databases merged. The resulting *uv* dataset was used as a starting point for the present study and the subsequent analysis by PWBR92 has not been used. Table 2 summarizes the observational set-up and global H I properties as derived from our work. All the data reduction was done using standard procedures in AIPS.

2.1. Multi-Configuration Data

We first rereduced the multi-configuration data of PWBR92 to optimize the sensitivity of the observations and to take advantage of the H I cloud detected to the southwest of the galaxy to extend as far as possible the kinematic information. The continuum was subtracted from the merged *uv* dataset using line-free channels and the AIPS task UVLIN, paying special attention to a strong continuum source at $\alpha = 8\text{h}17\text{m}05\text{s}$, $\delta = +70°52'29''.8$ (B1950). Given the small bandwidth used, HoII had no detectable continuum emission of its own (see, however, Tongue & Westpfahl 1995 for 90, 20, and 6 cm VLA observations).

Various tests were then performed using both uniform weighting, natural weighting, and various tapers and cleaning strategies. The application of a taper decreases the resolution without increasing much the detected flux, so a naturally weighted cube with no taper was produced (the cleaning was done with the AIPS task MX). This results in a beam of $14''.8 \times 14''.5$ and a rms noise per channel $\sigma = 1.1$ mJy beam^{-1}, essentially the same as PWBR92's medium resolution cube. This does not improve on the work of PWBR92, and the multi-configuration data will not be discussed further in light of the goals stated in the introduction. However, the fluxes published by PWBR92 must be revised down, due to complications when measuring fluxes of multi-configuration data. We discuss this issue below.

During our tests, it was noticed that the total flux in the cleaned maps decreased with increasing cleaning depth and/or increasing clean (restoring) beam size. This could be traced to a very non-Gaussian beam. Indeed, the beam yielded by the multi-configuration data is strongly peaked, and its effective area differs significantly from that of a Gaussian beam of equivalent resolution, resulting in bad total fluxes when the residuals and restored cleaned components of a map are summed (see Högbom 1974 for a description of the CLEAN algorithm). The fluxes converge for very deep cleaning, but this is impractical. Jörsäter & van Moorsel (1995) describe a simple corrective method to obtain reliable fluxes in such a situation. We applied this method to our multi-configuration naturally weighted data cube, channel by channel, to produce a clean (and corrected) cube with a cleaning depth of 1.5σ and a restoring beam of $15'' \times 15''$. The correction factor for the residuals in individual channels varied from 0.20 to 0.40, with a mean of 0.30. An identical cube without flux correction was also produced for comparison purposes.

Both cubes were used to produce moment maps, using a Gaussian smoothing of 2 spatially and Hanning smoothing over 3 channels spectrally. For all practical purposes, these moment maps are identical to those obtained by PWBR92 for their medium resolution data cube (see their Fig. 3 and 4). The cubes were also used to derive global profiles (after correcting for primary beam attenuation), summing the emission in each channel using the moment 0 map as a mask. The corrected and uncorrected profiles are shown in Fig. 1.

As expected, the shapes of the profiles are very similar, except at low fluxes where the contribution from residuals is non-negligible. The derived systemic velocities and velocity widths are identical and in agreement with those of Tully (1988): $V_{\odot} = 156 \pm 2$ km s^{-1}, $\Delta V_{50} = 57 \pm 3$ km s^{-1}, and $\Delta V_{20} = 72 \pm 3$ km s^{-1}. These also compare favorably with the global profile of PWBR92's medium resolution data cube, shown in their Fig. 2. On the other hand, the absolute fluxes of the three profiles differ substantially. The fluxes in our corrected cube are about 10% lower than those of the uncorrected cube ($F_{\rm HI} = 266$ and 294 Jy km s^{-1} respectively), in agreement with a correction factor less than unity for the residuals. This was to be expected since, before correction, the total flux decreased with increasing cleaning depth, suggesting that the residuals were overestimated. Had we cleaned less deep, the difference would have been even more important. PWBR92 report a total flux $F_{\rm HI} = 327$ Jy km s^{-1}, 10% higher than our *un*corrected cube. This can be explained by the different restoring beams used (PWBR92 used a $11\farcs0 \times 10\farcs9$ beam), that is, PWBR92 overestimated their residuals with respect to ours by a factor approximately equal to the ratio of the effective beam areas. Taking this into account, we can reproduce PWBR92's fluxes to within 1%.

This leaves no doubt that the corrective procedure proposed by Jörsäter & van Moorsel (1995) must be used to obtain reliable fluxes when dealing with complex beams, and that the fluxes derived from our corrected cube must be preferred over those of PWBR92. Single-dish total fluxes reported in the literature vary widely (Huchtmeier & Richter 1989 report values from $F_{\rm HI} = 164$ to 332 Jy km s^{-1}). Furthermore, given the very extended nature of the H I in HoII (as shown in the next section), even single-dish data could miss some emission, so it is difficult to estimate how much flux the synthesis observations are missing.

2.2. D-Array Data

As stated previously, the main reason behind a reanalysis of PWBR92's data was to maximize the sensitivity to large-scale structures. We thus created a new *uv* dataset containing the D-array data only, even though only 2 hours were spent observing in this configuration. The discussion in the rest of this paper focuses mainly on these data.

We first subtracted the continuum emission from the D-array *uv* dataset using line-free channels and the AIPS task UVLIN, as for the multi-configuration data. The emission extends approximately from $v_{\odot} = 105$ to 215 km s^{-1}. A naturally weighted cube with no taper was then created using the AIPS task MX. The resulting beam is $66.''7 \times 46.''4$ and the rms noise in the line-free channels $\sigma = 2.75$ mJy beam^{-1}. A cube cleaned to a depth of 1σ was then produced and reconvolved to a circular beam of $66.''7 \times 66.''7$. Because the central part of the original beam is well approximated by a Gaussian, the fluxes measured do not require correction.

Channel maps of the cleaned reconvolved cube are shown in Fig. 2. Only the largest bubbles and shells are now visible, due to the decreased spatial resolution compared to PWBR92's maps. The rotating disk pattern is still present, however, clearest at the extreme velocity channels, and the warp is revealed by a change of the kinematic major axis with radius. The most important feature of these maps is the large extent of the H I emission to the northwest of the galaxy. The H I extends to at least $16'$ from the center in certain channels, almost four times R_{25}. The H I cloud detected by PWBR92 is easily visible from $v_{\odot} = 175$ to 195 km s^{-1}, while it was absent from individual channel maps in the multi-configuration data cube.

The clean data cube was used to produce moment maps with the AIPS task MOMNT. These maps are shown in Fig. 3–5, superposed on an optical image of HoII. The same cube, corrected for primary beam attenuation, was used to calculate the global profile, summing the signal in each channel using the moment 0 map as a mask. The global profile is shown in Fig. 6.

The total H I map shown in Fig. 3, being at low-resolution, washes out a lot of the substructure visible in the maps of PWBR92, and provides us with an improved view of the large-scale structure of the H I in HoII. Undetected before, an extended but low surface brightness component is clearly visible to the north and northwest of the galaxy. The so-called H I cloud detected by PWBR92 to the southwest of the galaxy is also visible and appears to be part of the same structure as the H I detected to the northwest. Both components form a faint but large structure extending over the entire northwest half of the galaxy. Given that, in addition, the H I appears compressed at the southeast edge of the galaxy, this gives rise to a striking asymmetry between the southeast and northwest halves, the H I taking a comet-like appearance. This suggests that HoII may be affected by ram pressure from an IGM. We will discuss this issue further in § 4.

The faint structure discovered to the northwest is very important since it increases the area covered by H I by almost a factor of 2 compared to the work of PWBR92. The total extent of the H I now reaches $16'$ or $4R_{25}$ on the northwest side of the galaxy, twice the radius reached previously. This is a huge gain for studying the kinematics and mass distribution of the system.

The low-resolution velocity field shown in Fig. 4 clearly shows a differentially rotating disk pattern within at least the inner $\approx 7 - 8'$ in radius (albeit with an important warp). The situation is less clear in the faint outer structure. There, while the velocities are coherent with those slightly closer in (that is, there is no discontinuity between the velocities in the faint structure and those within the well-defined disk component), it is far from clear that we are dealing with a stable structure, and there may well be large non-rotational motions. We should thus expect difficulties to derive a rotation curve this far out. The closed isovelocity contours at about $4'$ from the center do indicate, however, that the rotation curve should peak around that radius.

The velocity dispersion field of HoII, shown in Fig. 5, displays numerous quasi-circular regions where the dispersion peaks. These are associated with expanding shells and were studied in details by PWBR92. The velocity dispersion in the disk of HoII is not constant at 8–10 km s^{-1}, but increases steadily toward the center. Over most of the optical disk, the dispersion is ≈ 15 km s^{-1}. Since the rotation velocity is $\sim 25/\sin i$ km s^{-1}, where i is the inclination of the disk, the dynamical support provided by the dispersion is not negligible over a large fraction of the disk, and it should be taken into account when modeling the mass distribution (the ratio of pressure to rotational support goes roughly as σ^2/v^2). This will be done in § 3 by correcting the derived rotation curve for asymmetric drift. The faint structure to the northwest has much smaller velocity dispersions, typically $\lesssim 7$ km s^{-1}.

The global profile of the D-array data, shown in Fig. 6, is very similar to those of the multi-configuration data shown in Fig. 1. The derived kinematical parameters are identical ($V_{\odot} = 156 \pm 2$ km s^{-1}, $\Delta V_{50} = 57 \pm 3$ km s^{-1}, and $\Delta V_{20} = 72 \pm 3$ km s^{-1}) and the total H I flux is almost the same as that of the corrected multi-configuration profile ($F_{\rm HI} = 267$ Jy km s^{-1}). This flux translates into a total H I mass of 6.44×10^8 $M_{\odot}$. The agreement between the D-array data and the corrected multi-configuration data supports the later and the correction method proposed by Jörsäter & van Moorsel (1995). Indeed, the simple beam of the D-array data leads to a more reliable flux determination. It also suggests that the D-array data is not missing much flux. However, given the very extended nature of the H I in HoII, this can only be confirmed with reliable *low* resolution single-dish data. Furthermore, the current extent of the H I reaches the half-power beam width (HPBW) of the VLA antennas ($\approx 32'$) to the northwest of the galaxy, so it is doubtful whether we could detect H I farther out even if it were there. Any follow-up observations of HoII with the VLA should use a mosaicing strategy.

3. Rotation Curve and Mass Modeling

3.1. Determination of the Rotation Curve

The rotation curve was derived using the velocity field shown in Fig. 4 and the now standard algorithm ROTCUR in AIPS (see Begeman 1987). ROTCUR models a rotating disk as a series of concentric inclined annuli, each annulus (radius r) having its own center (x_0,y_0), systemic velocity (V_{sys}), position angle (PA), inclination (i), and rotation velocity (v_{rot}). Given our beam of $66''.7 \times 66''.7$, we have chosen annuli of width $60''$ starting at $r = 60''$ (the inner $30''$ are thus unused). Data within $30°$ of the minor-axis were also rejected because of projection effects. ROTCUR yields formal errors, but modeling the approaching and receding sides of the galaxy separately often gives a more realistic idea of the uncertainties.

As a first step, we want to fix the center and systemic velocity of the galaxy to a common value for all the annuli. For this, we used only the inner $7 - 8'$ of the velocity field, where the rotating pattern is clearest. After various tests with all six parameters free and different initial guesses, the systemic velocity was fixed to 156.8 km s^{-1} (heliocentric), in agreement with the value obtained from the global profile, and the center was fixed to (α = 8h13m55s, $\delta = +70°52'52''$) (B1950), within one beam-width of the optical center. Leaving these 3 parameters fixed, we then derived a rotation curve for the inner parts of the velocity field only, using PA, i, and v_{rot} to minimize the residuals between the observed and modeled velocity fields. The position angle then varies from 168 to 213° and the inclination from 55 to 47°. This rotation curve is shown in Fig. 7. As the inclination we adopt is slightly higher than that of PWBR92, our rotation velocities are slightly lower (≈ 5 km s^{-1}).

As a final step, we derived the rotation curve using the entire velocity field. Given that the constraints on a possible dark matter halo become tighter with increasing radius, our aim was to extend the rotation curve to as large a radius as possible. It is clear however that the rotation pattern is very disturbed in the faint component to the northwest, making the derivation of a rotation curve to large radii non-trivial. ROTCUR on its own did not produce reliable fits in that region, so some manual intervention was required to obtain good solutions. We guided ROTCUR to a fit yielding a reasonably well-behaved rotation curve while keeping the residuals small. Clearly, this process is not entirely satisfactory, but it is the best that was possible given the data in hand. The position angle is fairly well constrained, but it is difficult to constrain reliably the inclination, particularly in the inner parts, because of the degeneracy between i and v_{rot}. Our adopted rotation curve is shown in Fig. 8, together with the variations of i and PA with radius. The values are tabulated in Table 3. As the data to the west are close to the minor-axis, it is the data to the north in the faint outer structure which contribute most to the rotation curve at large radii.

3.2. Asymmetric Drift Correction

The rotation curve just derived shows a clear break at about $r = 500''$, where the faint outer structure begins. This casts doubts about the reliability of the rotation curve past that point. However, as was pointed out before, because of the high velocity dispersion in the disk of HoII, it is likely that pressure support plays an important role. We must thus correct for the asymmetric drift in order to obtain a more reliable estimate of the circular velocity, truly representative of the underlying mass distribution.

The correction to the rotation curve can be written as

$$v_c^2 = v_{rot}^2 + \sigma_D^2, \tag{1}$$

where

$$\begin{aligned} \sigma_D^2 &= -r\sigma^2 \frac{\partial \ln(\rho\sigma^2)}{\partial r} \\ &= -r\sigma^2 \frac{\partial \ln(\Sigma\sigma^2)}{\partial r}, \end{aligned} \tag{2}$$

and v_c is the circular velocity, σ_D the asymmetric drift correction, ρ the volume density of H I, and Σ its surface density. The last line is obtained by assuming an exponential distribution in the vertical direction and a constant scaleheight.

To calculate the asymmetric drift correction, we thus need the surface density and velocity dispersion radial profiles. These can be easily obtained from the moment maps using azimuthal averages and the annuli adopted for the rotation curve fit (we must also assume a constant position angle PA=168° and inclination $i = 55\,\mathrm{deg}$). The resulting profiles are shown in Fig. 9, where the surface densities have been inclination-corrected. To obtain a smoother solution, we fit both σ^2 and $\Sigma\sigma^2$ with analytical functions. These profiles and the fitting functions are also shown in Fig. 9. σ^2 is well fitted by a Gaussian $\sigma^2(r) = I_0 \exp(-r^2/b^2)$, with $I_0 = 242$ km^2 s^{-2} and $b = 392''$. $\Sigma\sigma^2$ is well approximated by the function $\Sigma\sigma^2(r) = [I_0(R_0 + 1)]/[R_0 + \exp(\alpha r)]$, with $I_0 = 1350\ M_\odot$ pc^{-2} km^2 s^{-2}, $R_0 = 68''.3$, and $\alpha = 0.0159$ arcsec^{-1}. Using these functions, a smooth asymmetric drift correction can be calculated easily.

The rotation curve of HoII corrected for asymmetric drift is shown in Fig. 10, along with the actual correction applied and the uncorrected rotation curve. The numerical values are tabulated in Table 3. The sharp increase of the rotation velocities seen at $r \approx 500''$ in the uncorrected curve is much weaker in the corrected one; the jump is only 4–6 kms. This is because the asymmetric drift correction is most important in the radial range 200–700″, where the H I surface density drops most rapidly. The corrected rotation curve, our best estimate of the circular velocity curve, is not ideal for mass modeling, but it should allow us to roughly constrain the mass distribution.

3.3. Mass Modeling

The model we use to study the mass distribution of HoII is described in detail in Carignan (1985) and Carignan & Freeman (1985). This model calculates the mass contributions from the luminous component (stars and H I) and from a dark isothermal halo. To model the mass contribution of the stellar disk, the R-band luminosity profile (transformed into a B-band profile using the mean color $(B - R) = 0.767$; Swaters, private communication) is used with the assumption of a constant, unknown $(M/L_B)_*$. An intrinsic flattening $q_0 \equiv c/a = 0.12$ is adopted for the stellar disk (Bottinelli et al. 1983). For the H I component, we use the radial surface density profile of Fig. 9, multiplied by 4/3 to correct for the primordial Helium content. The dark halo component is represented by an isothermal sphere, described by two basic parameters: the core radius r_c and the one-dimensional velocity dispersion σ. The central density $\rho_0 = 9\sigma^2/4\pi G r_c^2$. The mass model therefore depends on three parameters: the amplitude scaling of the disk $(M/L_B)_*$, the radial scaling r_c, and the velocity scaling of the halo σ. In the fitting process, each point is weighted according to its error.

The "best-fit" model is shown in Fig. 11. Two reference radii need to be remembered: the optical radius, ≈ 4 kpc, and the radius up to which velocity points are present on both sides of the galaxy, ≈ 10 kpc. Up to the latter, we can consider the rotation curve to be well defined. For $10 \lesssim r \lesssim 18$ kpc, the rotation curve is only defined on the approaching side and one should be cautious when interpreting it. This is especially true in light of the discussion in § 4. The parameters that best fit the observed rotation curve are: the mass-to-light ratio of the stellar disk $(M/L_B)_* = 0.8$ and the core radius $r_c = 10$ kpc and one-dimensional velocity dispersion $\sigma = 23$ km s^{-1} of the dark isothermal halo. These correspond to a dark halo central density $\rho_0 = 0.00088\ M_\odot$ pc^{-3}.

It is interesting to note that the model fits the rotation curve very well both in the inner and outer parts, with the exception of the region around 10 kpc which marks the transition between the main body of the galaxy and the H I extension discovered in this study. If we restrain our analysis to the region of the rotation curve which is well defined ($r \lesssim 10$ kpc), it can be noted that the mass distribution of HoII is quite different from what is seen in most dwarfs and some late-type spirals, where dark matter dominates even within the optical radius (Carignan & Beaulieu 1989; Côté, Carignan, & Sancisi 1991; Côté, Carignan, & Freeman 2000). Here, dark matter contributes only $\approx 30\%$ of the mass within 4 kpc.

Considering the whole extent of the rotation curve (out to ≈ 18 kpc), we find a total mass of $6.3 \times 10^9\ M_\odot$, of which about 80% is dark ($M_{dark}/M_{lum} \approx 4.5$). This yields a total dynamical mass-to-light ratio $(M/L)_{dyn} \approx 16$. Now, similarly to what is seen in dwarfs and some late-type spirals, there is more luminous mass in H I than in stars (about a factor of 2). Thus despite some differences between HoII and most other dwarfs in the inner parts (luminous matter dominating within the optical radius), the system as a whole is completely dark matter dominated at the last point, *if we can trust the second half of the rotation curve.*

4. Ram Pressure and The Environment of HoII

4.1. Ram Pressure

Ram pressure, whereby the gaseous medium of a galaxy is stripped by its passage through a dense external medium, can be easily recognized by the typical morphology it imposes on the disturbed ISM (see, e.g., Stevens, Acreman, & Ponman 1999; Mori & Burkert 2000). Although it is hard to prove without doubt that ram pressure is responsible for any given disturbance in a galaxy, hot gas is known to be present in the center of many clusters and groups (Mulchaey 2000), so the ISM of galaxies on radial orbits will be affected to varying degrees. Evidence for ram pressure is also observed in many galaxies across a large range of wavelengths (see White et al. 1991 for optical, infrared, and X-ray observations of M86; Ryder et al. 1997 for optical and H I observations of NGC7421; Gruendl et al. 1993 for optical and Hα observations of NGC2276).

The threshold condition for ram pressure stripping can be written simply as

$$\rho_{\rm IGM} v^2 \geq 2\pi G \Sigma_{tot} \Sigma_g \tag{3}$$

(Gunn & Gott 1972), where the left side of the equation represents the pressure exerted by an intragroup medium (IGM) of density $\rho_{\rm IGM}$ on a galaxy moving at a relative velocity v, and the right side of the equation represents the restoring force of a disk with total surface density Σ_{tot} and gaseous (ISM) surface density Σ_g.

The faint structure observed in the outer parts of HoII, to the northwest, is suggestive of ram pressure. We can see from Fig. 3 that the H I disk starts to be perturbed at a flux level of $\approx 4.7 \times 10^{19}$ atoms cm^{-2}, corresponding to a deprojected H I surface density $\Sigma^i_{\rm HI} = 0.22\ M_\odot$ pc^{-2}. In our azimuthally averaged surface density profile (Fig. 9), this corresponds to a radius $r \approx 635''$. Assuming the optical disk to be exponential well past the last measured point, we can extrapolate the optical surface brightness profile of HoII to large radii. The fit to the outer parts of the disk by Swaters (1999) yields a central surface brightness $\mu_B(0) = 22.28$ mag arcsec^{-2} and a scalelength $h_B = 68\overset{''}{.}1$, or $\mu_B(r = 635'') = 32.4$ mag arcsec^{-2}, corresponding to a deprojected stellar surface density $\Sigma^i_* = 0.0042\ M_\odot$ pc^{-2} for $[(M/L)_B/(M/L)_{B,\odot}] = 1$. This is negligible compared to the H I surface density. We take $v \approx \sqrt{3}\sigma$ for the velocity of HoII with respect to a putative IGM, where σ is the line-of-sight velocity dispersion of the M81 group of galaxy. Estimates of σ in the literature, based on the central members of the group, are typically in the range $100 - 120$ km s^{-1}, so we adopt here the unweighted mean of a few values, $\sigma \approx 110$ km s^{-1} (see, e.g., Huchra & Geller 1982 and Garcia 1993), leading to $v \approx 190$ km s^{-1}. Correcting the neutral hydrogen surface density for other gaseous species, the IGM volume density required to strip the ISM of HoII at $r \approx 635''$ is, from Eq. (3), $n_{\rm IGM} \gtrsim 4.0 \times 10^{-6}$ atoms cm^{-3}. We assume everywhere media composed of 90% hydrogen and 10% He, yielding a mean mass per particle $\mu = 1.3 m_{\rm p}$ for neutral media and $\mu = 0.75 m_{\rm p}$ for fully ionized media ($m_{\rm p}$ is the proton mass).

Eq. (3) does not take into account the presence of a dark halo. However, if it interacts only through gravity and is not highly flattened, the dark halo should not significantly affect ram pressure, which acts mechanically and truly depends on the restoring force inside the disk. In the case of spiral galaxies, Abadi, Moore, & Bower (1999) show that the disk dominates the restoring forces to very large radii. They find good agreement between the analytic estimate of Gunn & Gott (1972) and their simulations, except at small radii where their bulge dominates. The dark halo will affect the evolution of the stripped material, in particular its fall back, as the entire potential of the galaxy is then important. Numerical simulations such as those discussed in § 5.3, which are concerned with the entire temporal evolution of the gas, do consider these effects (e.g. Quilis, Moore, & Bower 2000).

It is well known that the galaxies at the center of the M81 group are strongly interacting, with H I and optical bridges connecting the most massive members, and tails of H I extending to large radii (see, e.g., Cottrell 1977; Getov & Georgiev 1988; Yun, Ho, & Lo 1994). From the positions and radial velocities of the five most prominent spiral members of the group, Huchra & Geller (1982) derive a virial mass for the M81 group of $1.13 \times 10^{12}\ M_{\odot}$ (corrected to our adopted distance). This of course assumes that the group is bound, but since the virial crossing time of the group is much less than a Hubble time ($\approx 0.03\,H_0^{-1}$) and the central members are strongly interacting, this should be verified. HoII lies at the edge of the group, at a projected separation from M81 of about $8\overset{\circ}{.}5$ on the sky, corresponding to 475 kpc at the distance of HoII. If one assumes that 1% of the virial mass of the group is dispersed uniformly in a hot IGM within a sphere just enclosing HoII, the average IGM density within that volume would be 1.4×10^{-6} atoms cm^{-3}. This is only three times less than the IGM density required to strip the outer parts of the H I disk in HoII as calculated above (this assumes of course normal interacting baryonic matter).

While we do not claim the above number to be realistic, it does provide a benchmark with which to compare more sophisticated calculations. Any interaction debris would be strongly concentrated towards the center of the group and would be clumpy, reducing greatly the IGM density where HoII lies (hot gas, of course, is smooth). We have further considered a "face-on" encounter with the IGM, which is probably not the case given the morphology observed. On the other hand, since HoII is located at the very edge of the group, almost detached from it, it is quite possible that HoII is infalling for the first time, and it may well have a much larger velocity relative to the group than that assumed here. In fact, the outer parts of the group are probably not virialized. At a velocity of 190 km s^{-1}, HoII would take $\approx 2.4 \times 10^{9}$ yrs to reach the center of the M81 group. An infall scenario is further supported by the morphology of the H I gas, the tail pointing almost exactly away from the center of the group. In fact, since the group velocity dispersion adopted here is based only on a few large galaxies in the center of the group, it is most likely a lower limit. Including the fainter members of groups, whose orbits are less affected by dynamical friction and do not decay as rapidly, typically increases group velocity dispersions by at least 50% (up to a factor of 3; Zabludoff & Mulchaey 1998). This would reduce by at least a factor of two the IGM density required for ram pressure stripping. Most importantly, if one considers that HoII and/or other galaxies outside of the group's core are bound to the M81 group, than the virial mass assumed above is a serious underestimation, since only the 5 innermost large members were used in the calculations. If one assumes, for example, that the harmonic radius of the group encompasses HoII, then the derived viral mass and IGM density (as well as the crossing time) go up by a factor of at least 3.5. Any of these factors can thus bring the required and derived IGM densities in agreement with each other. In fact, from their spectroscopic survey of poor groups, Zabludoff & Mulchaey (1998) find that typical parameters of these groups are $R_{vir} \sim 0.5\,h^{-1}$ Mpc, $M_{vir} \sim 0.5 - 1 \times 10^{14}\,h^{-1}\ M_{\odot}$, and that only 10–20% of the mass is associated with individual galaxies. This leads to a mean density within that radius of $\approx 3.7 \times 10^{-3}$ atoms cm^{-3} for the remaining matter (for $H_0 = 75$ km s^{-1} Mpc^{-1}). Of course, most of that is probably non-baryonic, but on scales of the virial radius, the dominant baryonic component of the mass in group is the IGM (Mulchaey 2000). And while this is strictly true for X-ray bright groups only, where we can measure the gas content, it suggests at the very least that ram pressure can not be rejected without further analysis to explain the observed morphology of HoII at large radii.

4.2. X-Ray Gas in Small Groups

Ponman et al. (1996) have studied the X-ray properties of Hickson's compact groups of galaxies (Hickson 1982). A cursory examination of the M81 group shows that it meets all three criteria set by Hickson (indeed, it is not clear why the M81 group did not make it in the list). Ponman et al. (1996) detect X-ray emission in a large number of groups, including spiral rich groups, and infer that hot extended intragroup gas above their threshold of $L_x = 10^{41.1}$ erg s^{-1} is present in at least 75% of the groups (excluding emission from individual galaxies). The total X-ray luminosity of the groups does not correlate with either the total number of galaxies or optical luminosity, but it does correlate with the velocity dispersion and temperature (for Raymond & Smith 1977 plasmas). For a velocity dispersion of $\sigma = 110 \pm 10$ km s^{-1}, we obtain from the correlations of the combined group and cluster data of Ponman et al. (1996) $L_x = 10^{39.6\pm1.7}$ erg s^{-1} and $T_{\rm IGM} = 10^{-0.91\pm0.13}$ keV. However, there are indications that the correlations for the groups and clusters may be significantly different, and both of these numbers are probably underestimates. The large error on L_x is probably related to differences in the wind injection histories of the groups, as this can have a significant effect in small potential wells. In any case, it is clear that there could be a substantial amount of diffuse hot gas in the M81 group.

Helsdon & Ponman (2000a,b) carried out a similar study on a large number of loose groups. Using MEKAL hot plasma fits (Mewe, Lemen, & van den Oord 1986), they again obtained correlations between the temperatures, velocity dispersions, and X-ray luminosities of the groups. Using the loose groups correlations alone, we obtain $L_x = 10^{40.5\pm3.6}$ erg s^{-1} and $T_{\rm IGM} = 10^{-0.48\pm0.10}$ keV. Because the surface brightness profiles of groups can be quite flat, most likely because of the effects of winds, the reported luminosities are underestimates. For the coolest systems, the luminosity within a virial radius can be underestimated by more than a factor of two.

Helsdon & Ponman (2000a) also studied the surface brightness profiles of the groups, essential if we are to estimate the typical amount of hot gas present at the radius of HoII in a group like the M81 group. They fit the two-dimensional luminosity distributions with modified King functions

$$S(r) = S_0(1 + (r/r_c)^2)^{-3\beta+0.5}, \tag{4}$$

where S_0 is the central surface brightness, r_c the core radius, and β measures the steepness of the profile. Most groups require two such components to obtain a reasonable fit, but the three groups which are most similar to the M81 groups are all well fitted by a single-component. These are NGC 315, NGC 1587, and NGC 7777 (all three have four main members and $\sigma = 106 - 122$ km s^{-1}). Averaging their properties, we obtain $L_x = 10^{41.88\pm0.12}$ erg s^{-1}, $T_{\rm IGM} = 0.80 \pm 0.16$ keV (within the extracted radii), $r_c = 6.6 \pm 5.8$ kpc, $\beta = 0.73 \pm 0.56$, and $a/b = 1.16 \pm 0.21$ (elliptical fits). At large radii, Eq. (4) becomes $S(r) = S_0(r/r_c)^{-6\beta+1}$, and in the isothermal approximation the three-dimensional density profile then varies as

$$\rho(r) \propto (r/r_c)^{-3\beta}. \tag{5}$$

At a distance of 475 kpc, it is clear that these groups have very little IGM ($0.9 \pm 6.4 \times 10^{-4}$ of the density at the core radius). However, if the β–$T_{\rm IGM}$ trend observed by Helsdon & Ponman (2000a) for the higher quality (better statistics) two-component fits is "universal", then β for these groups could be significantly lower (by a factor of 2), leading to higher densities at large radii.

Another benchmark is provided by the study of poor groups of Zabludoff & Mulchaey (1998). They report typical X-ray gas masses of about $1 \times 10^{12}\,h^{-5/2}\ M_\odot$ for their groups, with virial radii $\sim 0.5\,h^{-1}$ Mpc. This leads to mean densities for the hot gas of $\approx 8.9 \times 10^{-5}$ atoms cm^{-3} within that radius. This is more than enough to strip the ISM in the outer parts of a galaxy like HoII, but is likely an overestimate for the density in the outer parts of the groups.

4.3. Gas Survival in a Hot IGM

4.3.1. The Effects of Shocks

Given the low spatial velocity of HoII, the IGM may or may not be shocked. With the range of temperatures allowed by the above correlations ($T_{\rm IGM} = 0.09 - 0.42$ keV, including the errors), the IGM sound speed $c_{\rm IGM} \approx (kT_{\rm IGM}/\mu m_{\rm p})^{1/2}$ km s^{-1} $\approx 110 - 230$ km s^{-1} (k is Boltzmann's constant; $c_{\rm IGM} \approx 320$ km s^{-1} for $T_{\rm IGM} = 0.80$ keV). Even if it is, the bow shock formed in front of HoII will barely affect post-shock conditions. Rankine-Hugoniot jump conditions for adiabatic shocks with $\gamma = 5/3$ imply an increase (respectively decrease) in the post-shock IGM density (respectively velocity) by a factor $M \approx v/c_{\rm IGM}$. The effect is thus always less than a factor of two and will be neglected in the following calculations. The estimates of viscous stripping are in any case unaffected since the product $\rho_{\rm IGM} v$ is conserved. The IGM density required for ram pressure stripping (see Eq. 3) would be increased by up to 75% for low IGM temperatures.

The H I in HoII certainly will be shocked, with a shock velocity $v_s \approx (n_{\rm IGM}/n_c)^{1/2}\, v \approx 0.4$ km s^{-1} at the critical IGM density required for ram pressure stripping (McKee & Cowie 1975). However, this does not heat the gas significantly ($T \approx 14\, v_s^2$ K).

4.3.2. The Stripped Material

Any gas stripped from the main body of HoII must survive long enough in the hot IGM to be observed. We follow here the discussion of Veilleux et al. (1999) in the case of NGC 4388. Neglecting radiation and magnetic fields, the evaporation timescale through thermal conduction for a cloud embedded in the IGM is

$$t_{evap} \approx 1 \times 10^3\, n_c R_{pc}^2\, (T_{\rm IGM}/10^7{\rm K})^{-5/2}\, (\ln\Lambda/30)\ \ {\rm yr} \tag{6}$$

(Cowie & McKee 1977), where n_c is the mean hydrogen cloud density in particles per cubic centimeter, R_{pc} the cloud radius in parsec, and Λ the Coulomb logarithm. For a typical cloud ($n_c \approx 1$ cm^{-3}, $R_{pc} \approx 10$ pc), the evaporation timescale is $6.2 \times 10^5 - 2.8 \times 10^7$ yrs (for $T_{\rm IGM} = 0.80$ keV, $t_{evap} \approx 1.2 \times 10^5$ yrs). The disturbed ISM observed in HoII extends over about $7 - 8'$ in projection in the radial direction. At a velocity of 190 km s^{-1}, it takes HoII about 3.6×10^7 yrs to cross that distance. Given the strong dependence of the evaporation on the assumed properties of the clouds and IGM, the timescales calculated seem compatible with the observations, at least for the lower IGM temperatures.

One could also speculate that the (presumably) stripped gas originates from the IGM itself. However, the cooling timescale for the IGM is

$$t_{cool} \approx 4 \times 10^6\, (T_{\rm IGM}/10^7{\rm K})^{3/2}\, (n_{\rm IGM}\, {\rm cm}^{-3})^{-1}\ \ {\rm yr} \tag{7}$$

(Rangarajan et al. 1995), which leads to $t_{cool} \approx 3.4 \times 10^{10} - 3.4 \times 10^{11}$ yrs at the IGM density required for ram pressure stripping ($t_{cool} \approx 9.0 \times 10^{11}$ yrs for $T_{\rm IGM} = 0.80$ keV). It is thus very unlikely that the gas condensed out of the hot IGM.

4.3.3. The HI Disk

The gaseous disk of HoII as a whole will also be subjected to various mass loss mechanisms due to the presence of a hot IGM. We follow here the discussion of Nulsen (1982) and consider in turn laminar viscous stripping, turbulent viscous stripping, and thermal evaporation. These can remove material from the disk even in regions not affected by ram pressure stripping.

Laminar viscous stripping leads to a mass loss

$$\dot{M}_{visc} \approx (12/\mathrm{Re})\,\pi R_{HI}^2 \rho_{\mathrm{IGM}} v, \tag{8}$$

where Re is the Reynolds number and R_{HI} is the (maximum) radial extent of the H I disk (we use here $R_{HI} = 16' = 14.9$ kpc). The classical treatment of viscosity requires that the ion mean free path in the IGM be sufficiently small, $\lambda_{\mathrm{IGM}} \lesssim R_{HI}$. In the absence of magnetic fields, $\lambda_{\mathrm{IGM}} \approx 11\,(T_{\mathrm{IGM}}/10^8\,\mathrm{K})^2\,(n_{\mathrm{IGM}}/10^{-3}\,\mathrm{cm}^{-3})^{-1}$ kpc $\approx 0.3-6.4$ kpc at the critical density needed for ram pressure stripping (Spitzer 1956; $\lambda_{\mathrm{IGM}} \approx 23.7$ kpc for $T_{\mathrm{IGM}} = 0.80$ keV). $\lambda_{\mathrm{IGM}} \lesssim R_{HI}$ is thus only marginally satisfied, although tangled magnetic fields would reduce it more. Laminar flows require Re $\lesssim 30$, but $\mathrm{Re} = 2.8\,(R_{HI}/\lambda_{\mathrm{IGM}})\,(v/c_{\mathrm{IGM}}) \approx 5-240$ (Batchelor 1967; Re = 1 for $T_{\mathrm{IGM}} = 0.80$ keV). The flow will thus unlikely be laminar, but turbulent, except possibly for a small range of intermediate T_{IGM}.

In a turbulent flow, Kelvin-Helmholtz instabilities will also generate mass loss at a rate

$$\dot{M}_{turb} \approx \pi R_{HI}^2 \rho_{\mathrm{IGM}} v \tag{9}$$

(Nulsen 1982). At the critical density required for ram pressure stripping, $\dot{M}_{turb} \approx 1.0 \times 10^{-2}\ M_\odot\ \mathrm{yr}^{-1}$. It would thus take 6.4×10^{10} yrs, much more than a Hubble time, to deplete the entire H I content of HoII with turbulent viscous stripping only. This process is thus unlikely to compete with ram pressure stripping, which removes the gas bodily from the galaxy. We recall that the time required for HoII to reach the center of the M81 group at a velocity of 190 km s^{-1} is 25 times smaller, $t_{cross} \approx 2.4 \times 10^9$ yrs. This suggests that if ram pressure was inefficient, HoII could cross the group many times without loosing its ISM.

The mass loss due to evaporation through thermal conduction is

$$\dot{M}_{evap} \approx 4\pi R_{HI}^2 \rho_{\mathrm{IGM}} c_{\mathrm{IGM}} \phi_s F(\sigma_0) \tag{10}$$

(Cowie & McKee 1977), where $\phi_s \approx 1$ and $\sigma_0 = 1.84\,\lambda_{\mathrm{IGM}}/R_{HI}\phi_s \approx 0.04-0.80$ ($\sigma_0 = 2.93$ for $T_{\mathrm{IGM}} = 0.80$ keV). $F(\sigma_0) \approx 2\sigma_0$ for $\sigma_0 \lesssim 1$, leading to $\dot{M}_{evap} \approx 1.7\times10^{-3}-7.8\times10^{-2}\ M_\odot\ \mathrm{yr}^{-1}$ ($4.0 \times 10^{-1}\ M_\odot\ \mathrm{yr}^{-1}$ for $T_{\mathrm{IGM}} = 0.80$ keV) and a depletion timescale for the H I in HoII of

$8.3 \times 10^9 - 3.7 \times 10^{11}$ yrs (1.6×10^9 yrs for $T_{\rm IGM} = 0.80$ keV). Except for very high $T_{\rm IGM}$, thermal evaporation is thus about as efficient as turbulent stripping to remove gas from the disk of HoII. However, even combined, these two mechanisms would still require a large fraction of a Hubble time to deplete the H I entirely.

We note that the "formalism" of turbulent viscous stripping applied here to the disk of HoII can equally be applied to our typical H I cloud, considered in the previous subsection. The timescale for complete viscous stripping can then be written as $t_{turb} = M_c/\dot{M}_{turb} \approx 4/3\,(R_c/v)(n_c/n_{\rm IGM})$, where M_c and R_c are the total mass and radius of the cloud, respectively. At the IGM density required for ram pressure stripping, this leads to $t_{turb} \approx 1.7 \times 10^{10}$ yrs, while we derived $t_{evap} \approx 6.2 \times 10^5 - 2.8 \times 10^7$ yrs ($t_{evap} \approx 1.2 \times 10^5$ yrs for $T_{\rm IGM} = 0.80$ keV). For the stripped material, therefore, evaporation is much more efficient than viscous stripping at removing gas.

Given the absence of extended X-ray emission associated with HoII (Zezas, Georgantopoulos, & Ward 1999), it is unlikely to possess a gaseous halo protecting it from the IGM, as suggested by Veilleux et al. (1999) in the case of NGC 4388. However, if the HoII, UGC 4483, and Kar 52 triplet or the NGC 2403 subgroup (see § 4.4 below) were to possess such a halo, then it could possibly offer some protection.

4.4. M81 and NGC 2403 Groups

While the morphology of the H I in HoII (Fig. 3) is reminiscent of that expected from ram pressure stripping, it could perhaps also be caused by an interaction. As mentioned before, the main galaxies at the center of the M81 group are known to be strongly interacting (see, e.g., Yun et al. 1994), and the "cometary" tail of H I could then represent material tidally stripped from the main body of HoII. However, HoII lies about 475 kpc from M81 (in projection), so it would take it at least one fifth of a Hubble time to reach the center of the group at a velocity of 190 km s^{-1}.

Figure 1 of van Driel et al. (1998) shows a map of the galaxies in the M81 group (their scale bar would be 0.4 Mpc at our adopted distance to HoII). HoII, along with Kar 52 (better known as M81 Dwarf A) and UGC 4483, appears to be part of a subsystem of three dwarf irregular galaxies to the northwest of the group's core. Kar 52 lies about 30 kpc to the northeast ($\Delta V_r \approx 40$ km s^{-1}), twice the maximum radial extent of the H I, and UGC 4483 is about 105 kpc to the southeast ($\Delta V_r \approx 0$ km s^{-1}). If HoII is interacting, it must be with one of these two galaxies. Figure 7 in Karachentsev et al. (2000) shows a larger map including the dwarf irregular galaxy NGC 2366, the dwarf spheroidal DDO 44, and the large spiral NGC 2403, to the west and southwest of HoII. These are sometime associated with the M81 group (e.g. de Vaucouleurs 1975) or may form a subgroup associated with NGC 2403.

Bremnes, Binggeli, & Prugniel (1998) present optical CCD images of both Kar 52 and UGC 4483. They are much smaller than HoII ($\approx 15 - 20\%$ at R_{25}) and are at least 4–5 magnitudes fainter. Both galaxies also have rather irregular optical morphologies, but neither shows obvious signs of interaction. UGC 4483 was recently studied with HST by Dolphin et al. (2001). Modeling of the color-magnitude diagram argues for a roughly constant star formation rate (SFR) of $1.3 \pm 0.2 \times 10^{-3}$ $M_{\odot}$ yr^{-1}, except for a young star cluster to the north ($\lesssim 100$ Myr), and the tip of the red giant branch yields a distance of 3.2 ± 0.2 Mpc. Kar 52 shows no sign of star formation (Miller & Hodge 1994), but no resolved stellar population study is available.

Kar 52 was first detected in H I by Lo & Sargent (1979) and was further studied by Sargent, Sancisi, & Lo (1983). The H I is distributed in a lumpy ring, incomplete to the northwest, which appears supported by turbulence (very little rotation is observed). If not for the fact that the broken ring appears to surround the optical galaxy, the morphology would again be very reminiscent of ram pressure. No H I is detected in the direction of HoII (to a column density of $\approx 10^{20}$ cm^{-2}), and there is no evidence of recent star formation. VLA and Westerbork H I observations of UGC 4483 are available in van Zee, Skillman, & Salzer (1998) and the WHISP database, respectively. The H I is centrally concentrated and the inner parts roughly follow the optical morphology, but a more extended, faint, and patchy component elongated NW–SE is also present. Only mild evidence of compression is observed at low levels on the southeast side, both in the total H I map and the velocity field.

Our adopted distance to HoII is identical to that of UGC 4483 (Dolphin et al. 2001), but also to the distances of NGC 2403 (Freedman & Madore 1988) and DDO 44 (Karachentsev et al. 1999). This suggests that HoII really belongs to the NGC 2403 subgroup, together with Kar 52, UGC 4483, NGC 2366, and DDO 44. Karachentsev et al. (2000) argue along the same lines. They show that the distance to the core of the M81 group is about 0.5 Mpc larger than that to the NGC 2403 subgroup, and that the mean radial velocity of the M81 group is *smaller* than that to the NGC 2403 subgroup. They thus suggest that the M81 and NGC 2403 groups (including HoII) are moving towards each other and estimate a relative velocity of 110–160 km s^{-1}.

The lack of evidence for interaction in the triplet of galaxies including HoII do not support this as the likely origin for its H I morphology. In fact, the H I observations of both Kar 52 and UGC 4483 are somewhat reminiscent of ram pressure. More sensitive

H I observations of the entire region around HoII, Kar 52, and UGC 4483 are necessary to clarify this issue. Distances to individual galaxies in the M81 group and NGC 2403 subgroup argue that HoII is part of the latter and may be moving towards M81 at a velocity of 110–160km s^{-1}, similar to or somewhat smaller than our adopted velocity of 190 km s^{-1}. Our calculations concerning ram pressure stripping thus do not depend strongly on whether HoII is bound to the M81 group or belongs to the NGC2403 subgroup and is infalling towards M81. In the latter case, an IGM more dense than what we have assumed (by up to a factor of 3) would be required to strip the ISM of HoII through ram pressure.

We note that H I synthesis observations of many other galaxies in the M81 group are available in the literature (see, e.g., Westpfahl et al. 1999). HoI and Kar 73, located closer to the group's core (but still well outside of the M81, M82, and NGC 3077 triplet), display disturbed morphologies not unlike those expected from ram pressure. At least for HoI, it appears as if the galaxy is falling towards the center of the group. Ott et al. (2001) discuss the possibility of ram pressure in this galaxy succinctly. Both HoI and Kar 73 were observed with the B, C, and D arrays of the VLA, but reanalyzing the D-array data only would be worthwhile, as we have done for HoII.

5. The Creation of Shells and Supershells

5.1. SNe and Stellar Winds

PWBR92 studied in details the numerous bubbles and shells present in the disk of HoII. Their main goal was to test whether these could be formed by SNe and stellar winds. We will briefly review their and following works here and highlight weaknesses of this scenario in the particular case of HoII.

PWBR92 identified and cataloged a large number of holes in HoII, measuring their positions, apparent sizes, ellipticities, and expansion velocities. These then yield simple estimates of the kinematic ages, previously enclosed H I masses, and creation energies of the holes. PWBR92 present various correlations between these properties, arguing for SNe and stellar winds as progenitors for the holes. However, many correlations presented are in fact a reflection of the physical properties of the host galaxy rather than of the creation mechanism of the holes, and many correlations that do depend on the creation mechanism could equally arise from a number of processes where the events are spread in time, cluster around a given energy, and where the most extreme events are rare. Support for the SNe and stellar wind scenario comes mainly, in our opinion, from the fact that at least some holes appear to be (roughly) spherically expanding and/or have a complete shell. Both of these properties point to internal pressure-driven events. Unfortunately, it is hard to gauge what fraction of the holes analyzed by PWBR92 really show such convincing evidence.

Contrary to what is claimed by PWBR92, we do no believe that their Hα image (their Fig. 21) strongly supports the SNe and stellar wind scenario. The Hα emission is not preferentially located at the edges of large holes, many walls in between holes showing no Hα emission at all, neither does it preferentially fill small holes, many of them showing no Hα either. Those properties are only verified in the very center of HoII. Furthermore, if SNe are indeed responsible for the formation of the largest holes, then these should by filled by hot X-ray gas ($\sim 10^6$ K), which has a long cooling time. However, pointed *ROSAT* PSPC and HRI observations of HoII analyzed by Zezas et al. (1999) reveal only a single unresolved X-ray source, coincident with a large H II region, and variable over a wide range of timescales. The bubbles in HoII therefore appear to be devoid of hot gas, and the X-ray emission which is seen probably arises from a compact accreting object. Kerp & Walter (2001) reanalyzed the *ROSAT* data, striving to reach the faintest fluxes possible. The X-ray emission observed is not preferentially associated with H II regions or H I holes, and a mixed bag of objects is detected at various locations within HoII. Of the 13 sources studied, 5 are located within H I holes, 4 in high column density regions, and 4 outside the stellar body of the galaxy. The latter detections are perhaps the most significant since they are likely SN remnants (SNRs) or X-ray binaries and suggest that star formation (SF) took place in the past well outside the regions where it is occurring now.

The issue of energy injection in the ISM is also crucial to the SNe and stellar wind scenario. Tongue & Westpfahl (1995) present multi-frequency radio continuum observations of HoII, allowing them to identify the dominant mechanism of radio emission in each structure observed. Of eight unresolved sources identified, only 3 have non-thermal emission probably associated with SNRs. Some diffuse emission consistent with non-thermal disk emission is also observed. The three probable SNRs are very strong, however, and they dominate the total flux. Tongue & Westpfahl (1995) show that the total SN rate required to form the bubbles in HoII (taken as the sum of the energy required to form the bubbles divided by the largest kinematic age and the typical energy output of a SNe) is in agreement with the total SN rate derived from the radio continuum emission (using three different methods, each associated with one emission mechanism). This suggest that the energy input from SNe alone can account for the substructure observed in the H I disk. However, as correctly pointed out by Tongue & Westpfahl (1995), the radio continuum maps correlate very well with the Hα image of PWBR92. This in turn means that they do *not* correlate well with the H I distribution. Indeed, the radio continuum emission is confined to the very inner parts of the H I distribution, away from most of the bubbles and shells. This suggest that the large energy output from SNe is not deposited at the right locations in the disk of HoII, hardly helping to identify the formation mechanism of the holes. Using numerical simulations, Mashchenko & Silich (1995) also tried to model the evolution of shells expanding under a local energy source in HoII, but numerous inconsistencies with the observations remained, in particular with respect to the elongation of the shells.

If the SNe scenario is right in the case of HoII, then about 25% of the holes cataloged by PWBR92 require more than 10 SNe to be created (up to 200). Given the ages of the bubbles ($10^7 - 10^8$ years), a significant population of A, F, and perhaps B-type stars should be left at the center of these holes (assuming a normal initial mass function). Rhode et al. (1999) obtained deep broadband BVR images of HoII to look for the remaining stellar clusters in all of the bubbles requiring at least one SNe. Unfortunately, useful constraints could only be derived for $\lesssim$ 30% of the holes, as the background light in the center of the galaxy is high and some holes need only harbor a small central cluster. In most cases where useful constraints are derived, the expected stellar clusters are simply not there, putting strong doubts on the validity of the SNe and stellar wind scenario for the formation of (at least) these holes. Stewart et al. (2000) also looked for the presumed SF and stellar populations at the origin of the holes, this time using far-ultraviolet (FUV) imaging (as well as UBR and Hα). FUV emission is sensitive to massive SF over a timescale comparable to the kinematic ages of the H I holes ($\lesssim$ 100 Myr), thus allowing to directly search for the holes' progenitors (Hα is only sensitive to very recent SF, $\lesssim$ 5 Myr). Stewart et al. (2000) find that the FUV emission is concentrated along the high density edges of the H I holes; no FUV knots are observed at the center of the shells. Only 3 of the 51 holes identified by PWBR92 appear to have associated FUV emission. In those three cases, the lower limit to the estimated mechanical energy output from the associated stellar clusters is systematically higher than that necessary to create the holes (but consistent in 2 cases). Furthermore, very little FUV emission is detected outside the inner $2 - 3'$, clearly indicating that the stellar wind and SNe scenario is not viable outside that region.

While the aforementioned studies seem to suggest that SF does depend on local conditions (i.e. the amount of shear), and while they weakly support some kind of sequential SF, they provide no smoking gun evidence that stellar winds and SNe are at the origin of the H I holes observed in HoII. The problem is most acute for the most energetic holes, which are generally located well outside of the optical extent of the galaxy. To a certain extent, the results of Tongue & Westpfahl (1995), Rhode et al. (1999), and Stewart et al. (2000) were to be expected since a cursory examination of the H I, optical broadband, and Hα images of HoII shows that many holes are located in low surface brightness regions of the disk, where no SF is expected or appears to be taking place.

We note that despite the fact that we have revised PWBR92's fluxes down by 23%, the problem of the high creation energies of the H I holes remains entirely. The estimated creation energy of a hole depends on the surface density at that point only quasi-linearly ($E_c \propto n_{\rm HI}^{1.12}$; Heiles 1979), therefore decreasing the values published by PWBR92 by 25% at most.

5.2. Alternative Explanations

While we do not wish to challenge the general relevance of SNe and stellar winds in shaping the ISM, the numerous shortcomings of this scenario in the specific case of HoII suggest that additional energy inputs and/or mechanisms are required to explain the observed substructure of the H I, particularly regarding the largest and most energetic holes located in the outer parts of the disk. Such a mechanism, ram pressure, is suggested by our reanalysis of PWBR92's data. Of course, numerous other processes exist which can explain the formation of bubbles and shells in galaxies, or can help to reconcile theoretical models with the observations just described. Rhode et al. (1999) discuss these at some length, so we only list them briefly here, and then focus in § 5.3 on how ram pressure may provide yet another explanation in the particular case of HoII.

The energies necessary to create the holes were calculated using the spherically-symmetric SNR model of Chevalier (1974), which assumes a uniform ISM. More complex models for both the SN evolution and/or the ISM could lead to lowered energies and decrease the flux expected from the progenitor clusters. A (extremely) top-heavy initial mass function (IMF) could also produce the required amount of SNe without an associated population of lower mass stars. Similarly, the blast waves associated with gamma-ray bursts, if caused by the collapse of a single massive star to a black hole, could create large holes in the ISM without requiring large stellar clusters. All these mechanism, however, still require massive SF to occur wherever there are holes, and this seems unlikely in the case of HoII. Other mechanisms bypass this requirement.

If the H I in galaxies is fractal (see, e.g., Westpfahl et al. 1999 for a study of the H I structure in M81 group galaxies), then holes may occur naturally through the same processes which create the fractal structure. A fractal H I would lead to significant changes in the energies required to create holes through SNe, as it would affect all heating and cooling timescales discussed in the previous sections. Elmegreen & Hunter (2000) also suggest that if giant H II regions observed in galaxies such as HoII are truly overpressured, then they should represent only a small fraction of the true population of H II regions ($\approx 7\%$; the timescale to reach pressure equilibrium being more than an order of magnitude larger than their present age). The unobserved old and faint H II regions could give rise, by merging, to large shells filling most of the disks and without recognisable associated clusters. Finally, the H I holes in the disk of HoII could be caused by ionization from an external source, such as the metagalactic UV radiation field (Bland-Hawthorn 1999), especially if the large scaleheight argued for by PWBR92 is confirmed.

High-velocity clouds (HVCs) also have the power to create large (cylindrical) holes in the ISM when impacting a disk. Holes in our galaxy and others have in fact been convincingly linked with high-velocity gas (see, e.g., Heiles 1984 for the Galaxy; van der Hulst & Sancisi 1988 for M101). Tenorio-Tagle (1980, 1981) discusses their formation and expansion. Rhode et al. (1999) explored this possibility in the case of HoII. They reexamined the low-resolution datacube of PWBR92 and identified one possible HVC. Although the detection is not statistically significant, the properties of the candidate cloud are interesting. Its emission extends over three velocity channels (the minimal criterion set by them) and about $90''$ spatially, with a total flux of 4.9 Jy km s^{-1}, yielding a total H I mass of 1.2×10^7 $M_\odot$. The cloud is located $17'$ to the southeast of HoII, at the edge of the VLA primary beam, and in the opposite direction from where we detect extended emission. It has a velocity relative to HoII of ≈ 65 km s^{-1}, giving it a kinetic energy of $\approx 5 \times 10^{53}$ ergs in HoII's rest frame. This is more than enough to create any of the holes observed. Clearly, many more less massive clouds, with the possibility of releasing $\lesssim 10^{52}$ ergs in the disk of HoII, could remain undetected.

5.3. Ram Pressure and the Creation of Shells

Ram pressure is a new ingredient that must be considered when studying the large- and small-scale structure of HoII. Ram pressure can create holes in a dense gaseous disk where local minima in the surface density exist. Together with viscous stripping, it also provides an efficient mechanism to enlarge pre-existing holes, created by SNe or otherwise, by ablating their edges. In the case of HoII, it could thus explain the surprisingly large creation energies of the holes and the lack of observational signatures expected from SNe and stellar wind scenarios. Unfortunately, no simulations or detailed calculations are available to verify the validity of this process quantitatively. The formation of holes through ram pressure should thus be modeled carefully before making any further claims.

It is interesting to note that in clusters with a deep potential well and/or a high gas density, the SFR of infalling disk galaxies can increase by up to a factor of two early on due to ram pressure compression of the molecular gas (Fujita & Nagashima 1999). The SFR decreases rapidly as the galaxy moves closer to the cluster center, however, due to stripping. As expected, the effect is less significant for shallower potential wells and/or lower gas densities. The tidal field of a cluster as a whole is also very efficient at triggering SF in disk galaxies, up to many core radii (Byrd & Valtonen 1990). It is unclear however how efficient these mechanisms can be in groups, where despite a less extreme environment the least massive disk galaxies (such as dwarf irregulars) could still be affected. Mori & Burkert (2000) do consider the effects of ram pressure and turbulent viscous stripping on dwarfs in clusters, but they consider a pressure supported extended hot ISM, so their results are not directly applicable to our situation. According to Mori & Burkert (2000), if HoII were to have a hot gaseous halo, it would not be stripped.

It should be possible observationally to distinguish ram pressure from internal, pressure-driven events such as SNe and stellar winds. One may expect the holes created from ram pressure to have a structure somewhat similar to that of a "bullet-hole", like that caused by the impact of a HVC. A one-sided shell should be created first, soon followed by an expanding cylindrical hole (e.g. Tenorio-Tagle 1980). In the case of ram pressure, however, one would also expect the characteristic tails of warm H I in pressure equilibrium with the intracluster medium (ICM) or IGM.

Quilis et al. (2000) present three-dimensional, self-consistent, N-body and hydrodynamical simulations of disk galaxies (with a bulge and dark matter halo) moving through a dense ICM. Not only do they consider different relative velocities, infall geometries, and ICM densities, but also different ISM distributions in the galaxy. Of particular interest to us, they consider gaseous disks with a large central hole or with numerous small holes distributed ramdomly throughout the inner parts. These mimic the central depletion of H I observed in many spiral galaxies and the numerous bubbles, shells, and holes present in spirals and dwarfs, be they created by SNe and stellar winds or otherwise. Compared to simulations with a homogeneous ISM, ram pressure stripping and viscous stripping are then much more efficient, removing material from the edges of the holes and preventing material from falling back on the galaxy. The morphologies obtained in the simulations compare advantageously with the H I distribution of HoII. We note that hydrodynamic codes unable to model viscosity and turbulence yield much smaller mass losses (e.g. Abadi et al. 1999). In all simulations, however, the timescale for gas depletion is much smaller than the crossing timescale of the cluster, so ram pressure acts very rapidly. This is consistent with HoII being on the outskirts of the M81 group, probably infalling for the first time.

The conditions in the simulations of Quilis et al. (2000) are not directly comparable to those in the M81 group or poor groups in general. However, while galactic velocities and intergalactic medium densities are both lower in groups (by an order of magnitude), typical disk surface densities in dwarfs are also much lower than in giant spiral galaxies.

The inequality in Eq. 3 may thus still be verified for dwarfs. The question is whether or not stripping occurs at a sufficiently small radius (or high H I surface density) to be detectable with current instruments. Simulations along these lines, taking into account the highly inhomogenous nature of the ISM in dwarfs, would be welcome.

6. Conclusions

With low resolution but sensitive VLA observations, we have shown that the large-scale structure of the H I disk in HoII is comet-like. Since HoII does not appear to be interacting with its neighbors and may be infalling towards to core of the M81 group, it is probably undergoing ram pressure stripping from an IGM. About 1% of the virial mass of the group must be contained in an IGM if the outer parts of HoII are to be stripped, consistent with X-ray observations of small groups. The length and morphology of the H I tail observed point to the additional effects of turbulent viscous stripping and thermal evaporation.

Ram pressure is interesting with regard to the creation of the H I holes in HoII. Since the expected traces of the implied SF are not observed, the creation energies of the holes through SNe and stellar winds must be systematically overestimated (or one must reject altogether this formation scenario). Ram pressure offers a mechanism to enlarge pre-existing holes, no matter how they were created, and thus lower their creation energies. A proof of the existence of a sufficiently dense IGM remains, however, the missing element to support this suggestion.

While detecting a diffuse hot IGM of density $10^{-6} - 10^{-5}$ atoms cm^{-3} would be very hard, especially in the M81 group given its large extent on the sky, it may be easier to look for other signatures of its presence. These include leading bow shocks (for galaxies moving supersonically through the IGM), gravitationally focused wakes, and the ram pressure stripped material itself (see Stevens et al. 1999). These may be detectable with the new generation of X-ray telescopes (*XMM* and *Chandra*) and could also be used to constrain the orbital structure (anisotropy) of the group (Merrifield 1998). HoII is a prime target for a search since it lies on the outskirt of a poor group with a presumably low IGM temperature. Contrary to expectations, the effects of ram pressure stripping are most easily visible in low surface brightness, cool, poor groups and clusters. In these, galaxies are able to retain a substantial fraction of their ISM, leading to prominent tails (see, e.g., Model 1b of Stevens et al. 1999)

Deep H I observations of the region around HoII, Kar 52, and UGC 4483 are also crucial. They could reveal evidence of interactions that were missed by the present observations and which could also explain HoII's large-scale morphology. They could also reveal or rule out the presence of dense, cold material in the vicinity of HoII (e.g. HVCs), which may be related to the creation of some of the holes. Observations along these lines are underway with the D configuration at the VLA.

We thank D. Puche for making available the reduced data of HoII. We also thank K. C. Freeman and J. H. van Gorkom for useful discussions. M. B. acknowledges the support of a Canadian NSERC Undergraduate Student Research Award, an Australian DEETYA Overseas Postgraduate Research Scholarship, and a NSERC Postgraduate Scholarship during various part of this work. Support for this work was also provided by NASA through Hubble Fellowship grant HST-HF-01136.01 awarded by Space Telescope Science Institute, which is operated by the Association of Universities for Research in Astronomy, Inc., for NASA, under contract NAS 5-26555. The Digitized Sky Surveys were produced at the Space Telescope Science Institute under U.S. Government grant NAG W-2166. The images of these surveys are based on photographic data obtained using the Oschin Schmidt Telescope on Palomar Mountain and the UK Schmidt Telescope. The plates were processed into the present compressed digital form with the permission of these institutions. The NASA/IPAC Extragalactic Database (NED) is operated by the Jet Propulsion Laboratory, California Institute of Technology, under contract with the National Aeronautics and Space Administration. This project also made use of the LEDA (www-obs.univ-lyon1.fr) and WHISP (http://www.astro.rug.nl/ whisp/) databases.

REFERENCES

Abadi, M. G., Moore, B., Bower, R. G. 1999, MNRAS, 308, 947

Batchelor, G. K. 1967, *An Introduction to Fluid Dynamics* (Cambridge: CUP)

Begeman, K. 1987, Ph. D. Thesis, Rijksuniversiteit Groningen

Bland-Hawthorn, J. 1999, in *Looking Deep in the Southern Sky*, eds. F. Marganti, & W. J. Couch (Berlin: Springer-Verlag), 91

Bottinelli, L., Gouguenheim, L., Paturel, G., & de Vaucouleurs, G. 1983, A&A, 118, 4

Bremnes, T., Binggeli, B., & Prugniel, P. 1998, A&AS, 129, 313

Brinks, E. 1981, A&A, 95, L1

Brinks, E., & Bajaja, E. 1986, A&A, 169, 14

Byrd, G., & Valtonen, M. 1990, ApJ, 350, 89

Carignan, C. 1985, ApJ, 299, 59

Carignan, C., & Beaulieu, S. 1989, ApJ, 347, 760

Carignan, C., & Freeman, K. C. 1985, ApJ, 294, 494

Chevalier, R. A. 1974, ApJ, 188, 501

Côté, S., Carignan, C., & Freeman, K. C. 2000, AJ, 120, 3027

Côté, S., Carignan, C., & Sancisi, R. 1991, AJ, 102, 904

Cottrell, G. A. 1977, MNRAS, 178, 577

Cowie, L. L., McKee, C. F. 1977, ApJ, 211, 135

Cox, D. P., & Smith, B. W. 1974, ApJ, 189, L105

Deul, E. R., & den Hartog, R. H. 1990, A&A, 229, 362

Dolphin, A. E., et al. 2001, MNRAS, 324, 249

van Driel, W., Kraan-Korteweg, R. C., Binggeli, B., & Huchtmeier, W. K. 1998, A&AS, 127, 397

Efstathiou, G. 2000, MNRAS, 317, 697

Elmegreen, B. G., & Hunter, D. A. 2000, ApJ, 540, 814

Freedman, W. L., & Madore, B. 1988, ApJ, 332, L63

Fujita, Y., & Nagashima, M. 1999, ApJ, 516, 619

Garcia, A. M. 1993, A&AS, 100, 47

Getov, R. G., & Georgiev, T. B. 1988, PAZh, 14, 811

Gruendl, R. A., Vogel, S. N., Davis, D. S., & Mulchaey, J. S. 1993, ApJ, 413, L81

Gunn, J. E., & Gott, J. R. III 1972, ApJ, 176, 1

Heiles, C. 1979, ApJ, 229, 533

——— 1984, ApJS, 55, 585

Helsdon, S. F., & Ponman, T. J. 2000a, MNRAS, 315, 356

——— 2000b, MNRAS, 319, 933

Hickson, P. 1982, ApJ, 255, 382

Högbom, J. A. 1974, A&AS, 15, 417

Huchra, J. P., & Geller, M. J. 1982, ApJ, 257, 423

Huchtmeier, W. K., & Richter, O.-G. 1989, *A General Catalog of H* I *Observations of Galaxies* (New York: Springer-Verlag) van der Hulst, J. M. 1996, in *The Minnesota Lectures on Extragalactic Neutral Hydrogen*, ed. E. D. Skillman (San Francisco: ASP), 47

van der Hulst, T., & Sancisi, R. 1988, AJ, 95, 1354

Jörsäter, S., & van Moorsel, G. A. 1995, AJ, 110, 2037

Kamphuis, J. J. 1993, Ph.D. Thesis, Rijksuniversiteit Groningen

Karachentsev, I. D., et al. 1999, A&A, 352, 399

——— 2000, A&A, 363, 117

Kerp, J., & Walter, F. 2001, in *X-ray Astronomy 2000*, eds. R. Giacconi, L. Stella, & S. Serio (San Francisco: ASP), in press

Lo, K. Y., & Sargent, W. L. W. 1979, ApJ, 227, 756

Mashchenko, S. Y., & Silich, S. A. 1995, ARep, 39, 587

Merrifield, M. R. 1998, MNRAS, 294, 347

Mewe, R., Lemen, J. R., & van den Oord, G. H. J. 1986, A&AS, 65, 511

McKee, C. F., & Cowie, L. L. 1975, ApJ, 195, 715

McKee, C. F., & Ostriker, J. P. 1977, ApJ, 218, 148

Miller, B. W., & Hodge, P. 1994, ApJ, 427, 656

Mori, M., & Burkert, A. 2000, ApJ, 538, 559

Mulchaey, J. S. 2000, ARA&A, 38, 289

Nulsen, P. E. J. 1982, MNRAS, 198, 1007

Ott, J., Walter, F., Brinks, E., Van Dyk, S. D., Dirsch, B, & Klein, U. 2001, AJ, in press (astro-ph/0110154)

Ponman, T. J., Bourner, P. D. J., Ebeling, H., & Böhringer, H. 1996, MNRAS, 283, 690

Puche, D., Westpfahl, D., Brinks, E., & Roy, J.-R. 1992, AJ, 103, 1841 (PWBR92)

Quilis, V., Moore, B., & Bower, R. 2000, Science, 288, 1617

Rangarajan, F. V. N., White, D. A., Ebeling, H., & Fabian, A. C. 1995, MNRAS, 277, 1047

Raymond, J. C., & Smith, B. W. 1977, ApJS, 35, 419

Rhode, K. L., Salzer, J. J., Westpfahl, D. J., & Radice, L. A. 1999, AJ, 118, 323

Ryder, S. D., Purcell, G., Davis, D., & Andersen, V. 1997, PASA, 14, 81

Sargent, W. L. W., Sancisi, R., Lo, K. Y. 1983, ApJ, 265, 711

Silich, S. A., Franco, J., Palouš, J., Tenorio-Tagle, G. 1996, ApJ, 468, 722

Spitzer, L., Jr. 1956, *Physics of Fully Ionized Gases* (London: Wiley)

Stevens, I. R., Acreman, D. M., & Ponman, T. J. 1999, MNRAS, 310, 663

Stewart, S. G., et al. 2000, ApJ, 529, 201

Swaters, R. 1999, Ph. D. Thesis, Rijksuniversiteit Groningen

Tenorio-Tagle, G. 1980, A&A, 88, 61

———. 1981, A&A, 94, 338

Tenorio-Tagle, G., & Bodenheimer, P. 1988, ARA&A, 26, 145

Tongue, T. D., & Westpfahl, D. J. 1995, AJ, 109, 2462

Tully, R. B. 1988, *Nearby Galaxies Catalog* (New York: CUP)

de Vaucouleurs, G. 1975, in Galaxies and the Universe, eds. A. Sandage, M. Sandage, & J. Kristian (Chicago: University of Chicago Press), 557

Veilleux, S., Bland-Hawthorn, J., Cecil, G., Tully, R. B., & Miller, S. T. 1999, ApJ, 520, 111

Westpfahl, D. J., Coleman, P. H., Alexander, J., & Tongue, T. 1999, AJ, 117, 868

White, D. A., Fabian, A. C., Forman, W., Jones, C., & Stern, C. 1991, ApJ, 375 35

Yun, M. S., Ho, P. P. T., & Lo, K. Y. 1993, Nature, 372, 530

Zabludoff, A. I., & Mulchaey, J. S. 1998, ApJ, 496, 39

van Zee, L., Skillman, E. D., & Salzer, J. J. 1998, AJ, 116, 1186

Zezas, A. L., Georgantopoulos, I., & Ward, M. J. 1999, MNRAS, 308, 302

This preprint was prepared with the AAS LaTeX macros v4.0.

Fig. 1.— Global profiles of HoII derived from the multi-configuration data. *Filled circles:* Profile corrected for the non-Gaussian beam shape. *Empty circles:* Uncorrected profile.

Fig. 2.— Channel maps of HoII for the D-array data cube. Levels are 3, 10, 20, 40, 60, and 80 times 2.5 mJy beam^{-1} (1σ = 2.75 mJy beam^{-1}). Positions are B1950 and the heliocentric velocity of each channel is indicated in the top-right corner of each map. The beam is $66\farcs7 \times 66\farcs7$, indicated in the bottom-left corner of the first map on each page.

Fig. 3.— Total H I map of HoII for the D-array data, superposed on a Digitized Sky Survey image. Contours are 0.1, 0.3, 0.6, 1.0, 2.0, 4.0, 6.0, 10.0, 13.0, 16.0, and 19.0 times 10^{20} atoms cm^{-2} or 16.8 $M_{\odot}$ pc^{-2}). The closed contours centered at approximately (α = 8h12m06s, $\delta = +70°51'05''$), (α = 8h13m15s, $\delta = +70°51'20''$), (α = 8h13m48s, $\delta = +70°55'05''$), (α = 8h13m52s, $\delta = +70°50'45''$), (α = 8h14m00s, $\delta = +70°53'45''$), and (α = 8h14m25s, $\delta = +70°55'25''$) represent density decrements. The beam is $66\farcs7 \times 66\farcs7$.

Fig. 4.— H I velocity field of HoII for the D-array data, superposed on a Digitized Sky Survey image. Contours are 120, 130, 135, 140, 150, 160, 170, 175, and 180 km s^{-1}. The closed contours centered at approximately (α = 8h14m00s, $\delta = +70°49'00''$) and (α = 8h13m50s, $\delta = +70°57'00''$) have velocities of 135 and 175 km s^{-1} respectively. The beam is $66\farcs7 \times 66\farcs7$.

Fig. 5.— H I velocity dispersion field of HoII for the D-array data, superposed on a Digitized Sky Survey image. Contours are 6, 9, 12, 15, 18, and 21 km s^{-1}. The beam is $66\farcs7 \times 66\farcs7$.

Fig. 6.— Global profile of HoII derived from the D-array data.

Fig. 7.— Rotation curve of HoII for the inner velocity field only ($r \lesssim 8'$). The errors represent half the difference between the rotation curves of the approaching and receding sides of the galaxy taken separately.

Fig. 8.— *Top panel:* Adopted variation of PA with radius. *Middle panel:* Adopted variation of i with radius. *Bottom panel:* Adopted rotation curve of HoII for the entire velocity field. The errors represent half the difference between the rotation curves of the approaching and receding sides of the galaxy taken separately. There is no error bar past $r = 660''$ as the rotation curve was determined for the approaching side only past that point.

Fig. 9.— *Top panel:* Radial profile of the deprojected H I surface density Σ in HoII. *Second panel:* Radial profile of the H I (line-of-sight) velocity dispersion σ. *Third panel:* Radial profile of σ^2. *Bottom panel:* Radial profile of $\Sigma\sigma^2$. The solid lines are the fits to the data discussed in the text (§ 3.2).

Fig. 10.— *Filled circles:* Rotation curve of HoII corrected for asymmetric drift. *Empty circles:* Uncorrected rotation curve. *Solid curve:* Asymmetric drift correction. The errors represent half the difference between the rotation curves of the approaching and receding sides of the galaxy taken separately. There is no error bar past $r = 660''$ because the rotation curve was determined for the approaching side only past that point. No error for the asymmetric drift correction was included.

Fig. 11.— Mass model of HoII. The contributions of the 3 components are shown: the stellar disk, H I disk, and dark isothermal halo. In order not to give too much weight to the outer points only defined on the approaching side, the mean error from the inner points was used.

Table 1. Basic Properties of HoII

Quantity	Value	Reference
Right ascension (B1950)	$\alpha = 8\text{h}14\text{m}00\overset{\text{s}}{.}5$	1
Declination (B1950)	$\delta = +70°52'29''.8$	1
Heliocentric velocity	$V_{\odot} = 156$ km s^{-1}	2
Distance	$D = 3.2$ Mpc	3
Morphological type	Im	4
Conversion factor	$1'' = 15.5$ pc	
Total apparent B magnitude	$m_{B_T} = 11.13$ mag	1
Corrected apparent B magnitude	$m^{0,1}_{B_T} = 10.51$ mag	1
Total absolute B magnitude	$M_{B_T} = -17.01$ mag	
Apparent radius ($\mu_B = 25$ mag arcsec^{-2})	$R_{25} = 4'.1$	1
Apparent axial ratio ($\mu_B = 25$ mag arcsec^{-2})	$b/a = 0.87$	1

References. — (1) Lyon/Meudon Extragalactic Database; (2) This work; (3) PWBR92; (4) NASA/IPAC Extragalactic Database.

Table 2. D-Array H I Observations of HoII

Quantity	Value
Date of Observations	1991 March 6
Total bandwidth	1.56 MHz
Channel width	2.58 km s^{-1}
Heliocentric central velocity	190 km s^{-1}
Primary beam (HPBW)	$\approx 32'$
Synthesized beam (FWHM)	$66\overset{''}{.}7 \times 46\overset{''}{.}4$
rms noise in channel maps	2.75 mJy beam^{-1}
Conversion factor (1 mJy beam^{-1})	0.14 K
Total H I Flux	$F_{\rm HI} = 267$ Jy km s^{-1}
Total H I Mass	$M_{\rm HI} = 6.44 \times 10^8\ M_\odot$
H I Velocity Width	$\Delta V_{50} = 57$ km s^{-1}
	$\Delta V_{20} = 72$ km s^{-1}
Total Mass (within $r \approx 20' = 18.6$ kpc)	$M_{\rm tot} = 6.3 \times 10^9\ M_\odot$

Table 3. HoII D-Array Rotation Curve Parameters

r (arcsec)	PA (degree)	i (degree)	v_{app} (km s^{-1})	v_{rec} (km s^{-1})	v_{rot} (km s^{-1})	σ_D (km s^{-1})	v_c (km s^{-1})
60	168	55	15.82	16.71	16.28	2.87	16.53
120	168	55	24.10	25.26	24.67	6.14	25.42
180	168	55	26.80	27.16	26.98	10.68	29.02
240	168	55	28.80	26.88	27.84	15.90	32.06
300	177	55	29.55	26.17	27.93	20.14	34.43
360	177	44	30.27	25.37	27.80	22.03	35.47
420	177	44	27.32	22.70	25.05	21.68	33.13
480	177	44	31.23	24.81	29.34	19.92	35.46
540	201	73	33.81	23.58	31.08	17.48	35.66
600	201	73	39.25	26.13	37.09	14.80	39.93
660	201	73	40.64	31.46	40.08	12.14	41.88
720	201	73	39.99	···	39.97	9.69	41.13
780	201	84	38.71	···	38.71	7.52	39.43
840	180	84	37.38	···	37.38	5.68	37.81
900	180	84	38.38	···	38.38	4.19	38.61
960	180	84	39.12	···	39.12	3.00	39.24
1020	180	84	39.86	···	39.86	2.10	39.92
1080	180	84	39.06	···	39.06	1.43	39.09
1140	180	84	38.10	···	38.10	0.95	38.11
1200	180	84	38.46	···	38.46	0.62	38.46

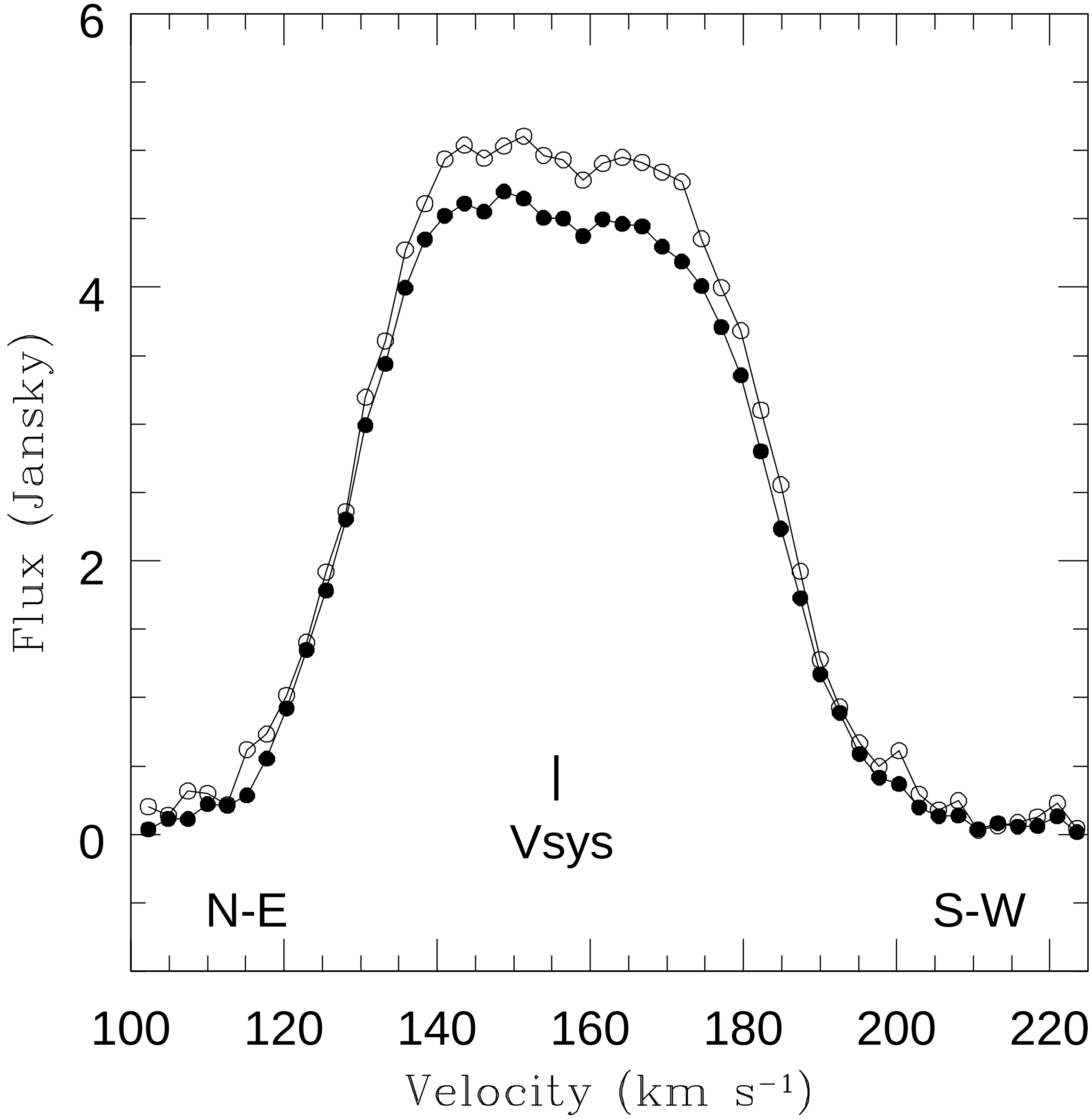
6
4
2
0
Flux (Jansky)
100
120
140
160
180
200
220
Velocity (km s^{-1})
Vsys
N-E
S-W

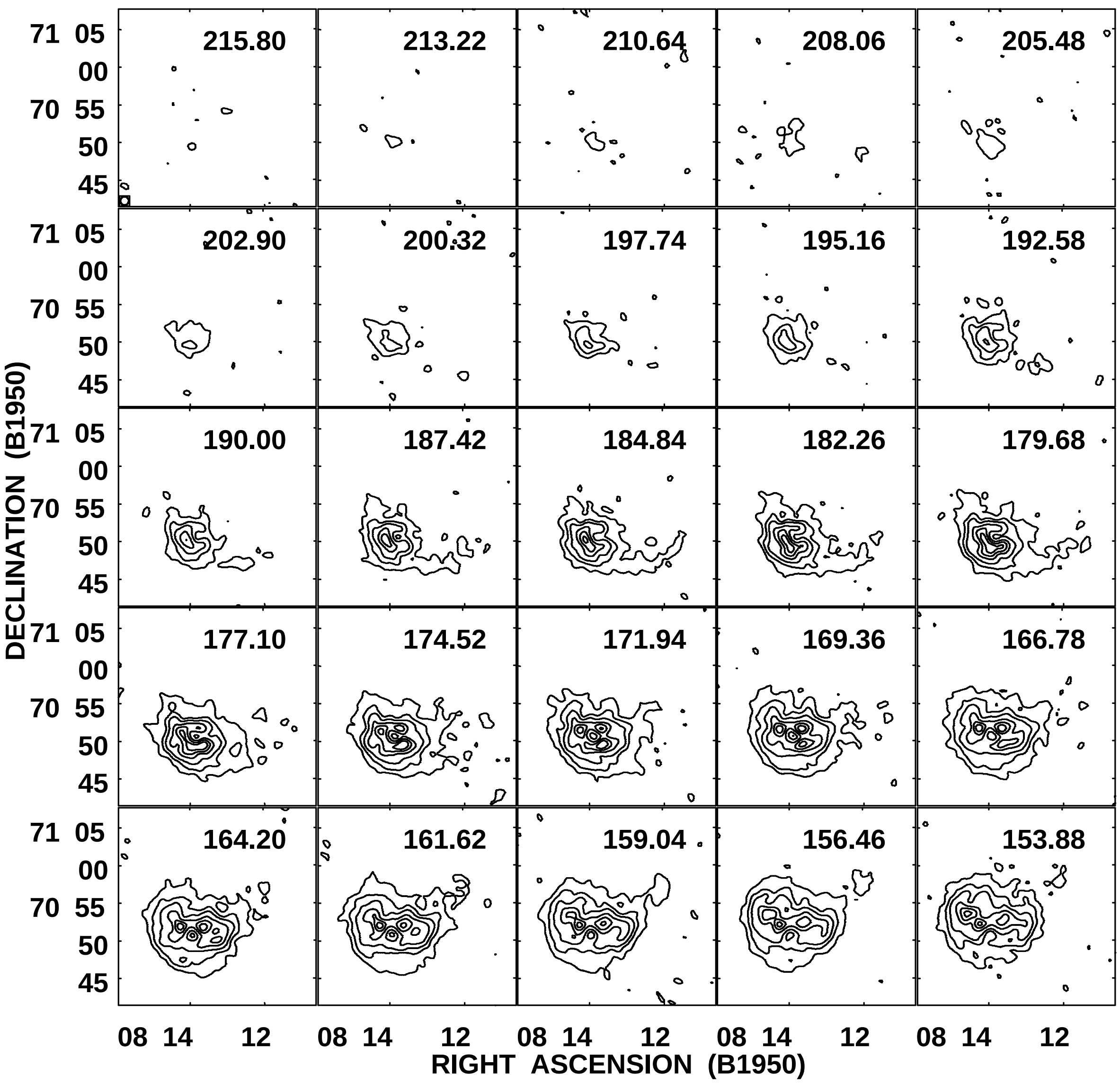
215.80
213.22
210.64
208.06
205.48
202.90
200.32
197.74
195.16
192.58
190.00
187.42
184.84
182.26
179.68
177.10
174.52
171.94
169.36
166.78
164.20
161.62
159.04
156.46
153.88
DECLINATION (B1950)
71 05
00
70 55
50
45
RIGHT ASCENSION (B1950)
08 14
12

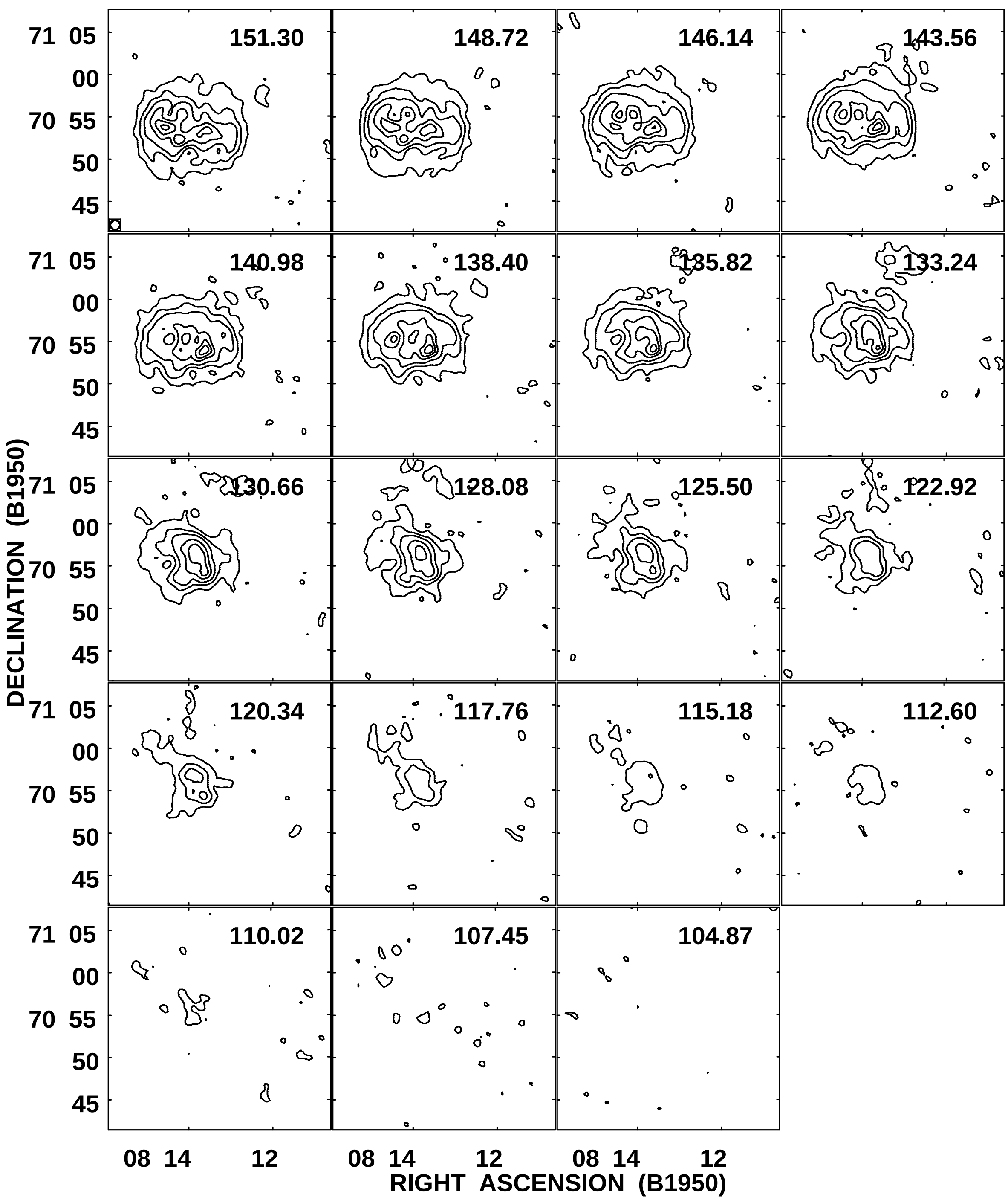

151.30
148.72
146.14
143.56
140.98
138.40
135.82
133.24
130.66
128.08
125.50
122.92
120.34
117.76
115.18
112.60
110.02
107.45
104.87
71 05
00
70 55
50
45
DECLINATION (B1950)
08 14
12
RIGHT ASCENSION (B1950)

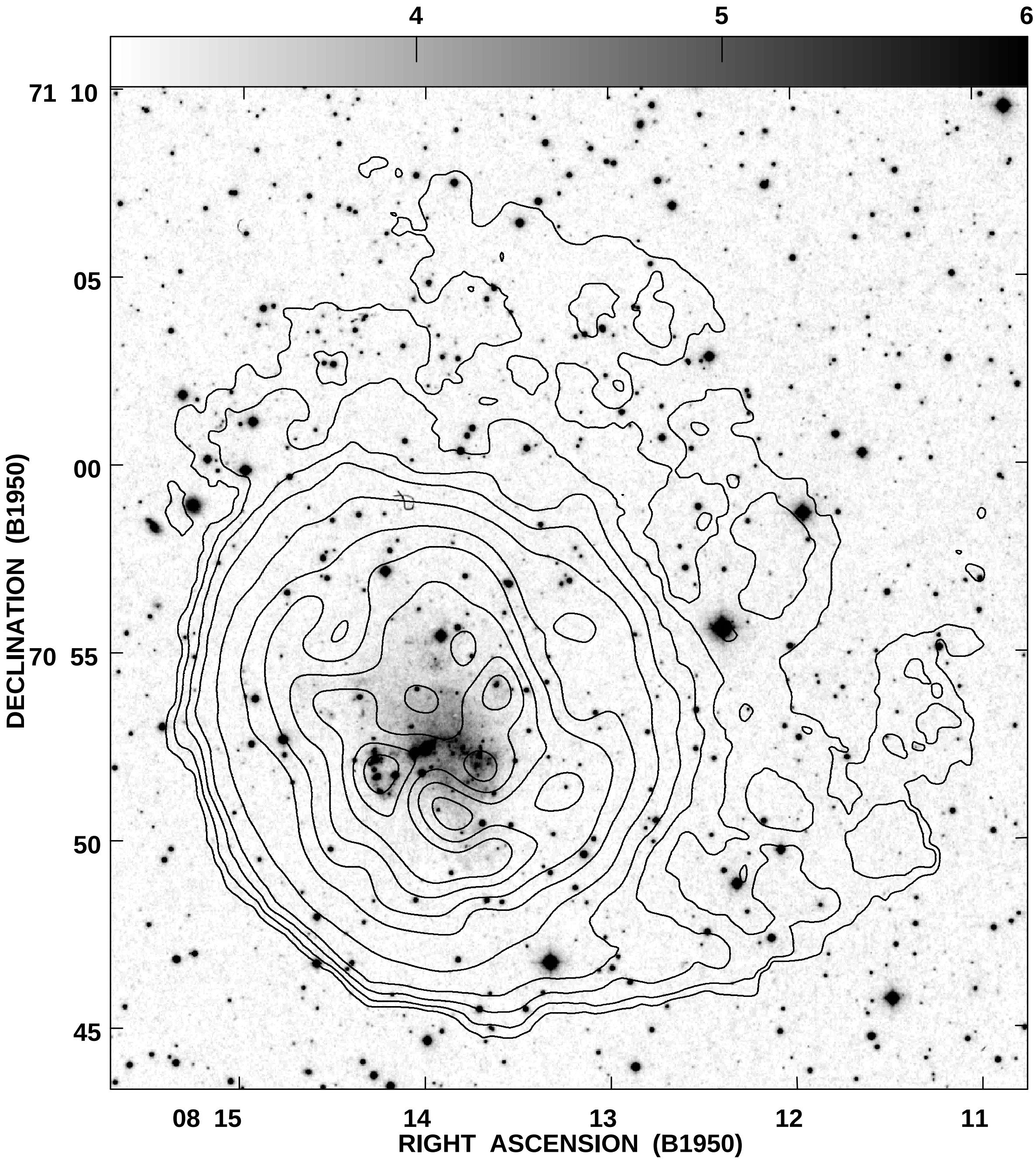
4
5
6
71 10
05
00
70 55
50
45
DECLINATION (B1950)
08 15
14
13
12
11
RIGHT ASCENSION (B1950)

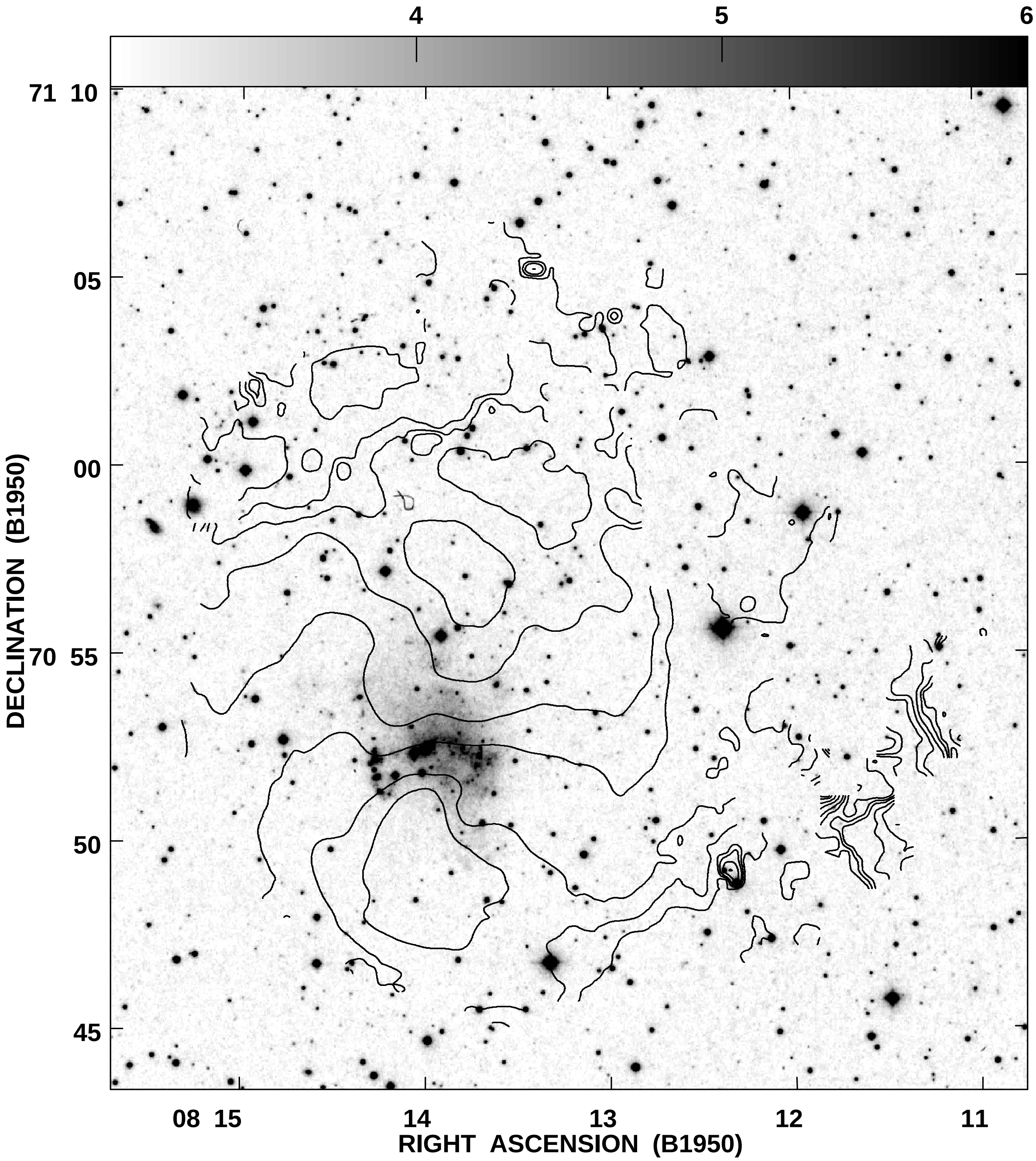
4
5
6
71 10
05
00
70 55
50
45
DECLINATION (B1950)
08 15
14
13
12
11
RIGHT ASCENSION (B1950)

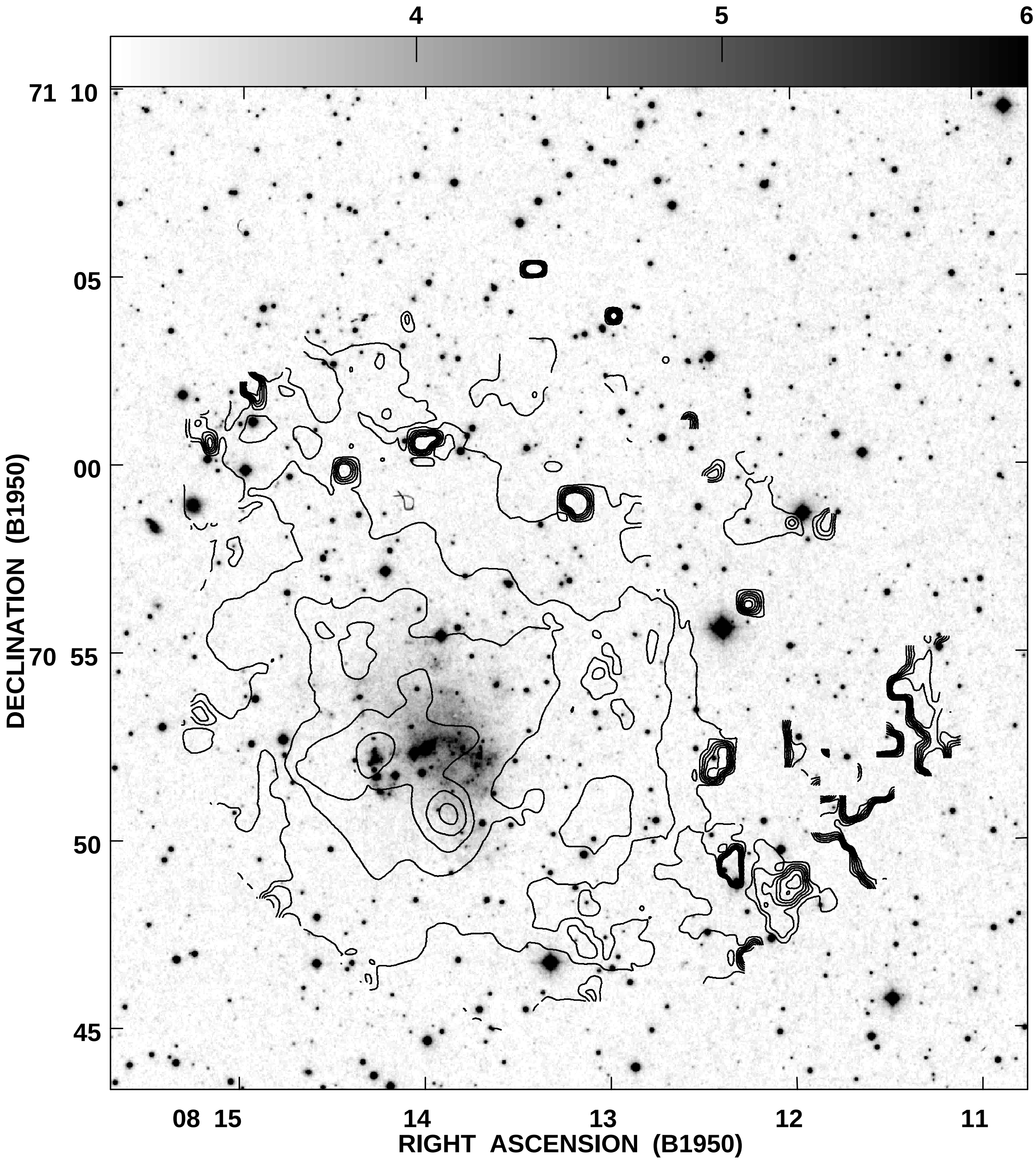
4
5
6
71 10
05
00
70 55
50
45
DECLINATION (B1950)
08 15
14
13
12
11
RIGHT ASCENSION (B1950)

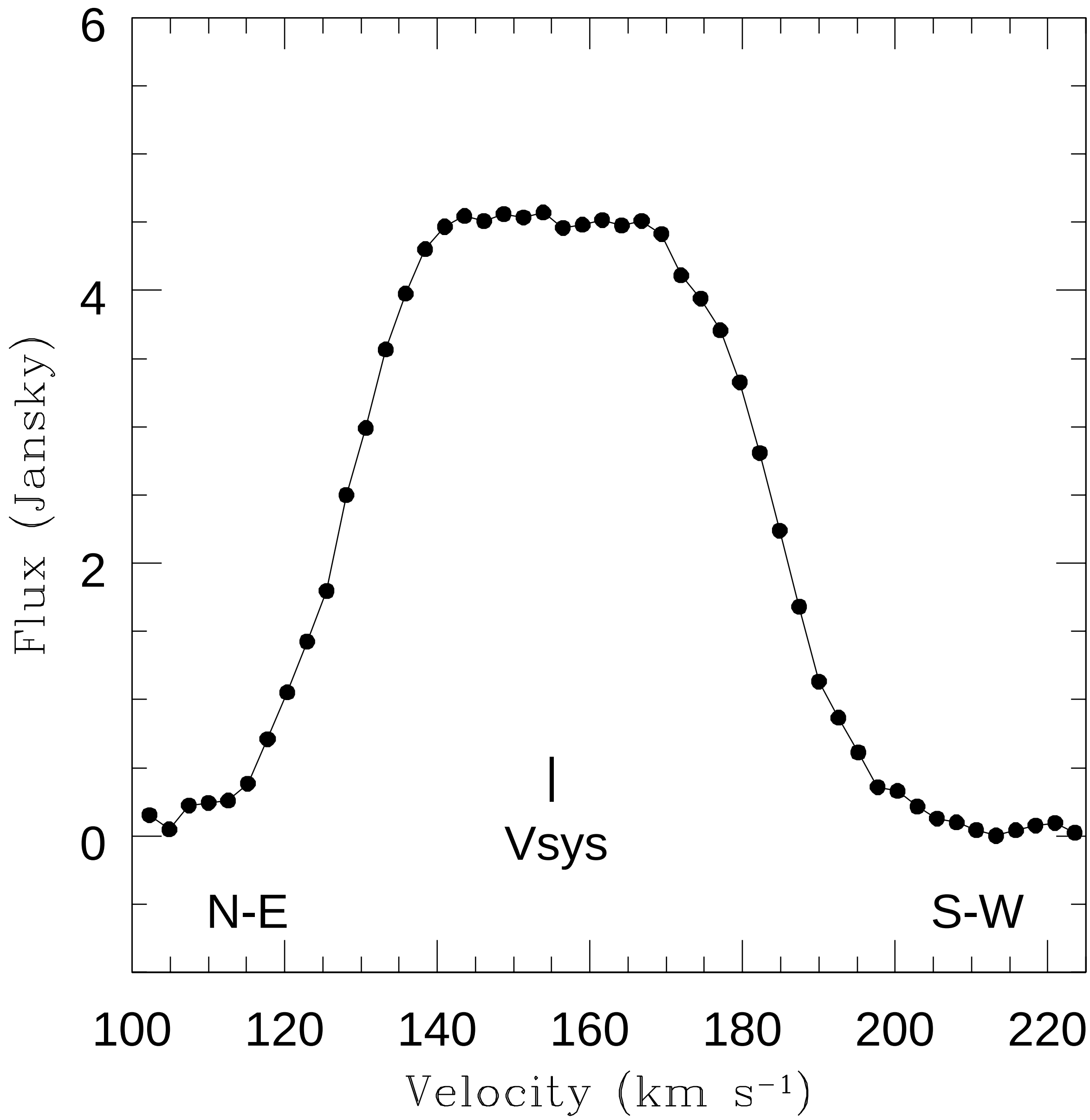
6
4
2
0
Flux (Jansky)
100
120
140
160
180
200
220
Velocity (km s⁻¹)
Vsys
N-E
S-W

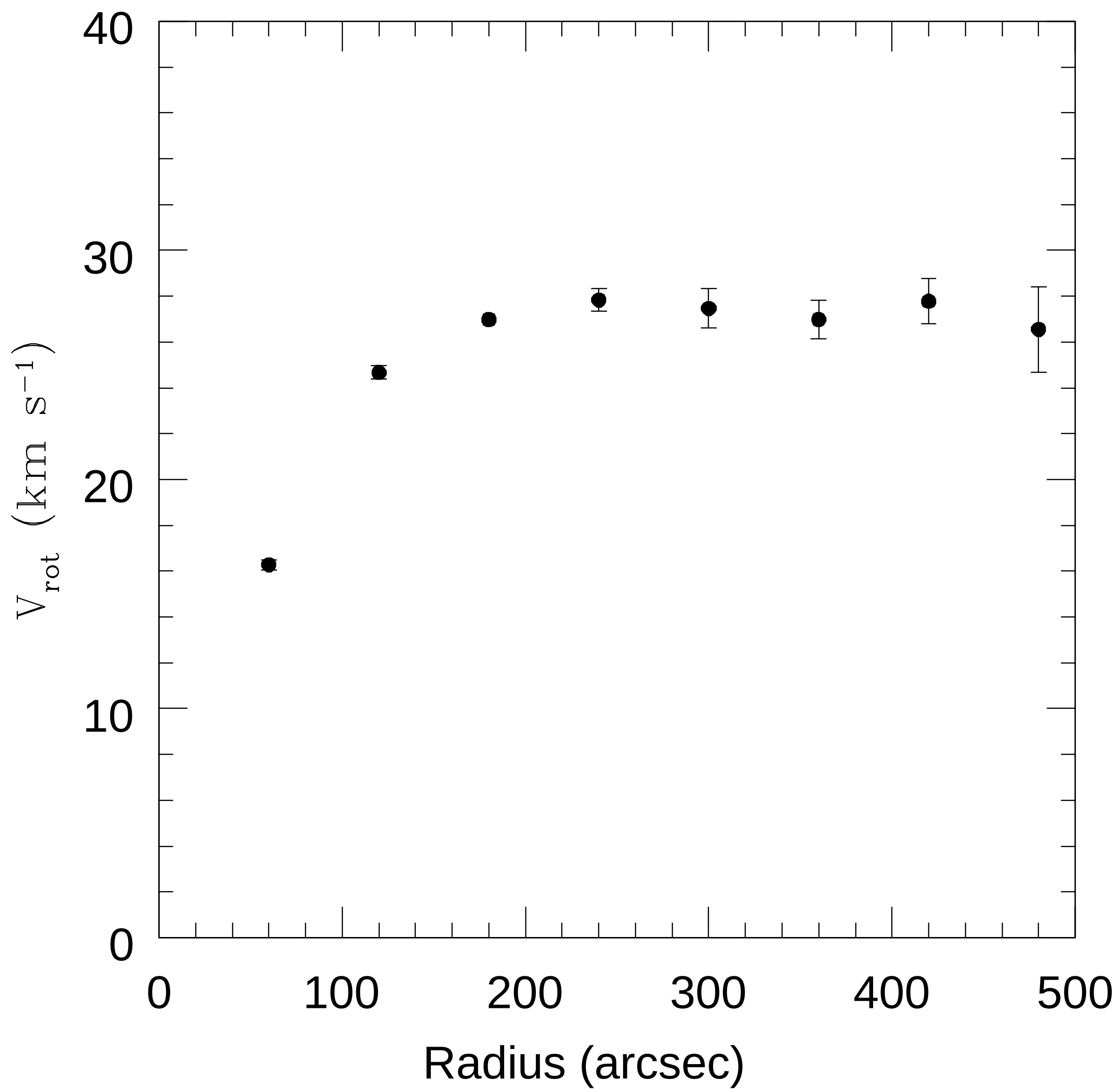
40
30
20
10
0
0
100
200
300
400
500
Radius (arcsec)
V_{rot} (km s^{-1})

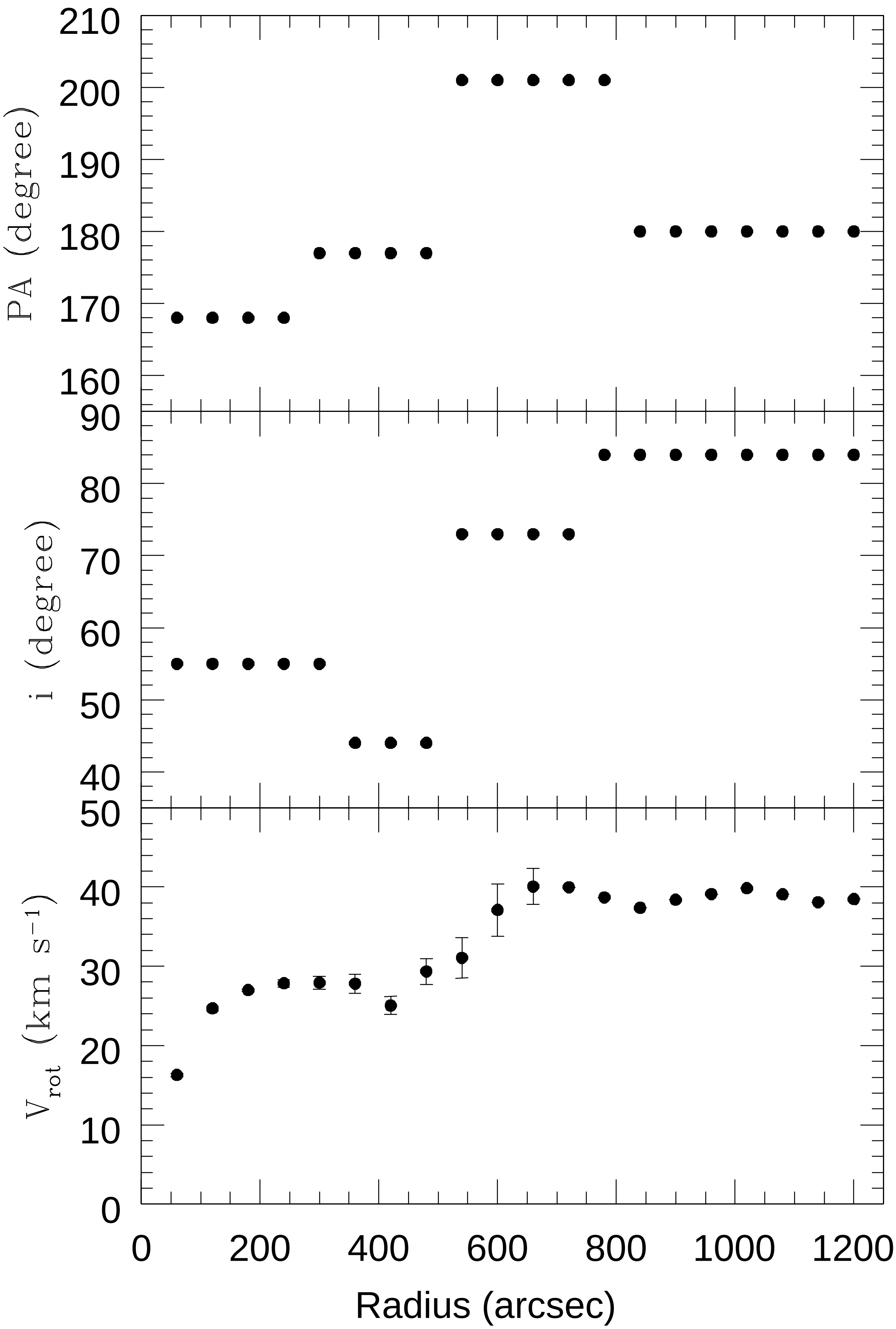
210
200
190
180
170
160
PA (degree)
90
80
70
60
50
40
i (degree)
50
40
30
20
10
0
V_{rot} (km s^{-1})
0
200
400
600
800
1000
1200
Radius (arcsec)

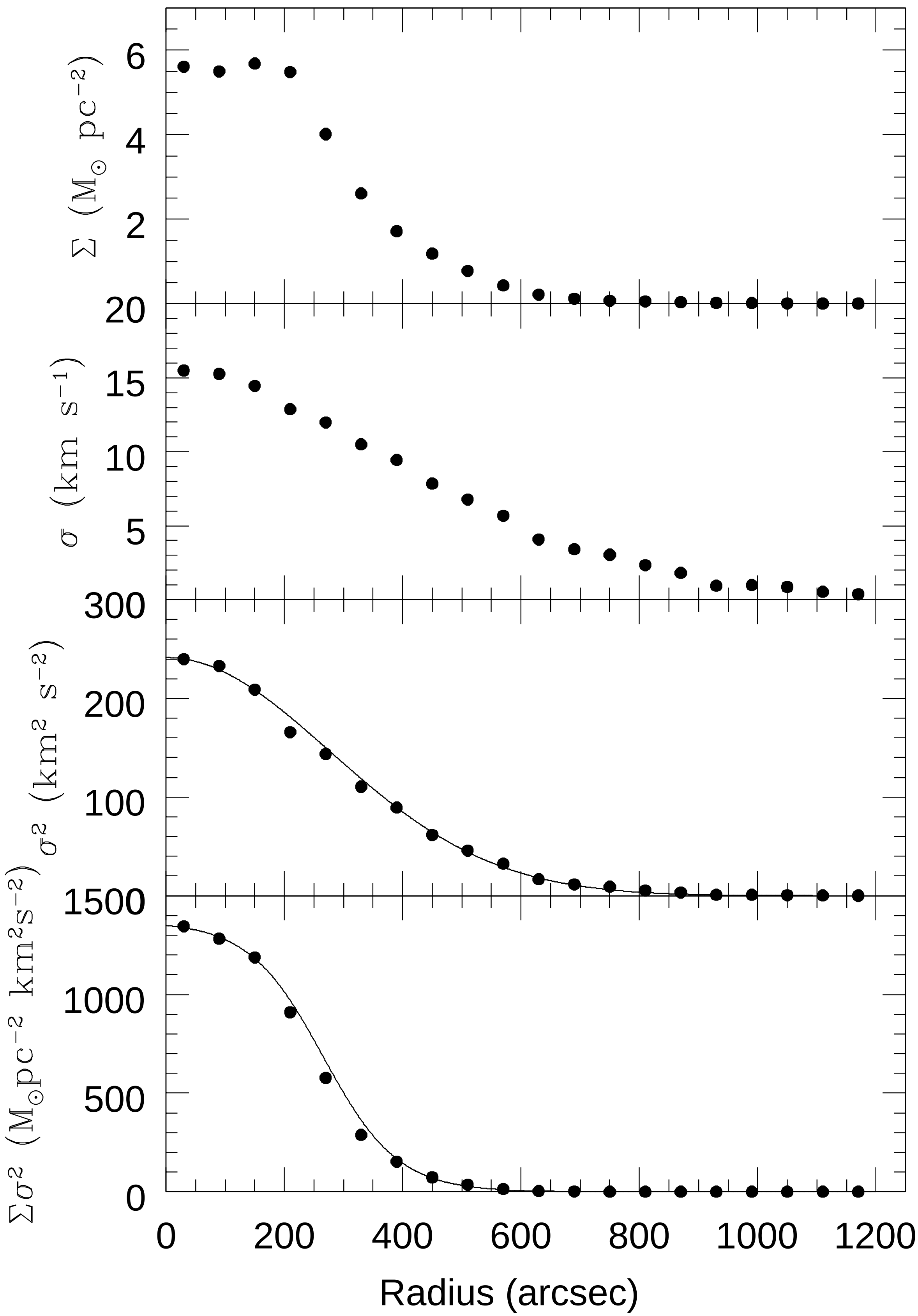

Σ (M⊙ pc⁻²)
6
4
2
20
15
10
5
σ (km s⁻¹)
300
200
100
σ² (km² s⁻²)
1500
1000
500
0
Σσ² (M⊙pc⁻² km²s⁻²)
0
200
400
600
800
1000
1200
Radius (arcsec)

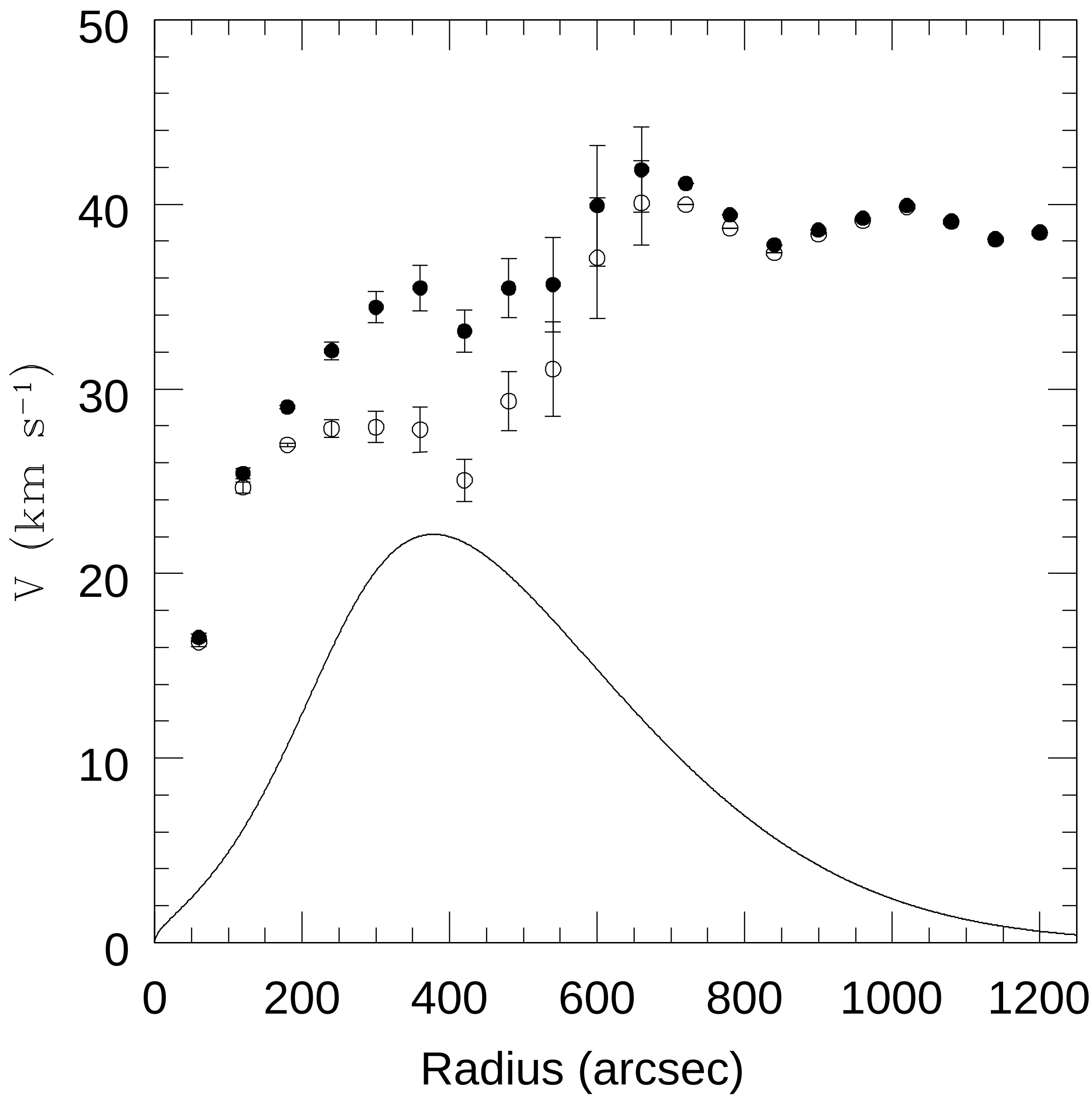
50
40
30
20
10
0
V (km s^{-1})
0
200
400
600
800
1000
1200
Radius (arcsec)

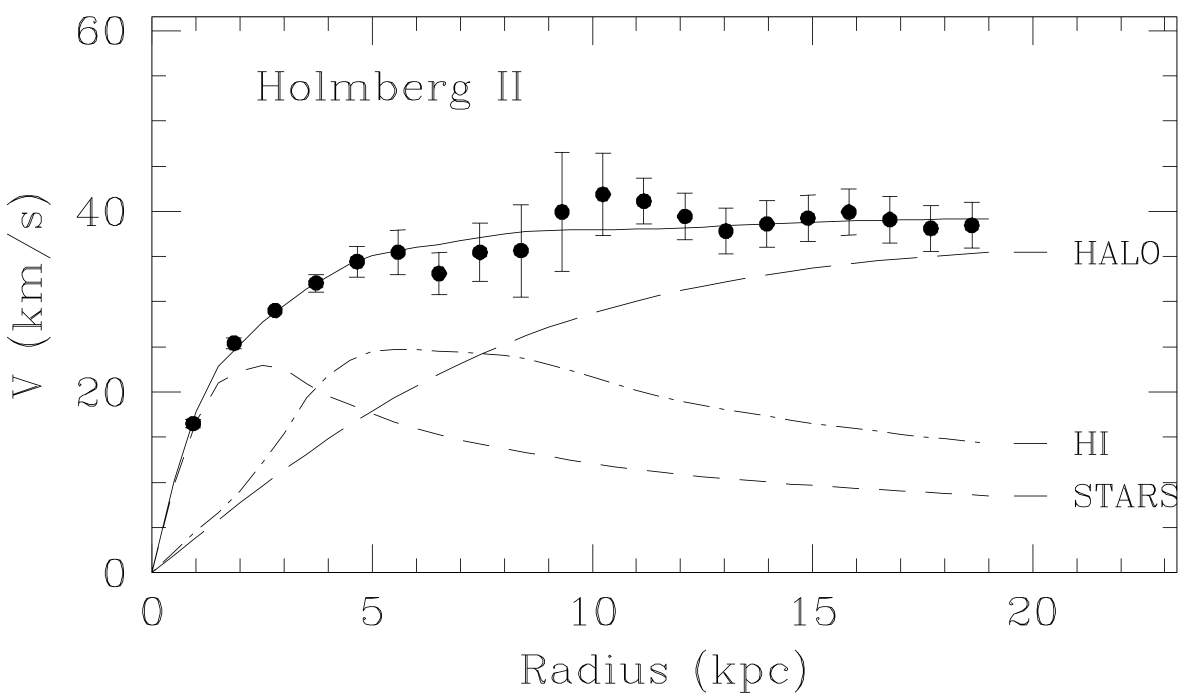
Holmberg II
V (km/s)
Radius (kpc)
HALO
HI
STARS
0
20
40
60
0
5
10
15
20